Characterizing Drought Behavior using Unsupervised Machine Learning for Improved Understanding of Future Drought in the Colorado River Basin

Carl James Talsma[1], Katrina E. Bennett[1], and Velimir V Vesselinov[2]

[1]Los Alamos National Lab
[2]Los Alamos National Laboratory (DOE)

November 22, 2022

Abstract

Drought is a pressing issue for the Colorado River Basin (CRB) due to the social and economic value of water resources in the region and the significant uncertainty of future drought under climate change. Here, we use climate simulations from various Earth System Models (ESMs) to force the Variable Infiltration Capacity (VIC) hydrologic model and project multiple drought indicators for the sub-watersheds within the CRB. We apply an unsupervised machine learning (ML) based on Non-Negative Matrix Factorization using K-means clustering (NMFk) to synthesize the simulated historical, future, and change in drought indicators within the sub-watersheds. The unsupervised ML approach can identify sub-watersheds where key changes to drought indicator behavior occur, including shifts in snowpack, snowmelt timing, precipitation, and evapotranspiration. While changes in future precipitation vary across ESMs, the results indicate that the Upper CRB will experience increasing evaporative demand and surface-water scarcity, with some locations experiencing a shift from a radiation-limited to a water-limited evaporation regime in the summer. Large shifts in peak streamflow are observed in snowmelt-dominant sub-watersheds, with complete disappearance of the snowmelt signal for some sub-watersheds. Overall, results indicate a concerning increase in drought risk. The work demonstrates the utility of the NMFk algorithm to efficiently identify behavioral changes of drought indicators across space and time. Our unsupervised ML approach can be applied to other spatiotemporal data to process and understand vast arrays of data associated with climate impacts analysis of hydrologic change, assisting planners to rapidly assess potential risks associated with extreme events.

Characterizing Drought Behavior using Unsupervised Machine Learning for Improved Understanding of Future Drought in the Colorado River Basin

Carl J. Talsma[1], Katrina E. Bennett[1], Velimir V. Vesselinov[1]

[1] Earth and Environmental Sciences, Los Alamos National Laboratory, Los Alamos, NM, 87545.

Corresponding authors: Carl J. Talsma(talsmac83@lanl.gov), Velimir V. Vesselinov (vvv@lanl.gov)

Key Points:

- Unsupervised machine learning automatically identifies key sub-watersheds with significant changes in their future drought indicators.
- In the Colorado River Basin mountains, distinct differences in future streamflow seasonality and intensity changes are established.
- Significant uncertainty in drought behavior is observed among the applied climate models.
- Colorado River Basin sub-watersheds with threshold changes in maximum evaporation are identified.

Abstract

Drought is a pressing issue for the Colorado River Basin (CRB) due to the social and economic value of water resources in the region and the significant uncertainty of future drought under climate change. Here, we use climate simulations from various Earth System Models (ESMs) to force the Variable Infiltration Capacity (VIC) hydrologic model and project multiple drought indicators for the sub-watersheds within the CRB. We apply an unsupervised machine learning (ML) based on Non-Negative Matrix Factorization using K-means clustering (NMFk) to synthesize the simulated historical, future, and change in drought indicators within the sub-watersheds. The unsupervised ML approach can identify sub-watersheds where key changes to drought indicator behavior occur, including shifts in snowpack, snowmelt timing, precipitation, and evapotranspiration. While changes in future precipitation vary across ESMs, the results indicate that the Upper CRB will experience increasing evaporative demand and surface-water scarcity, with some locations experiencing a shift from a radiation-limited to a water-limited evaporation regime in the summer. Large shifts in peak streamflow are observed in snowmelt-dominant sub-watersheds, with complete disappearance of the snowmelt signal for some sub-watersheds. Overall, results indicate a concerning increase in drought risk. The work demonstrates the utility of the NMFk algorithm to efficiently identify behavioral changes of drought indicators across space and time. Our unsupervised ML approach can be applied to other spatiotemporal data to process and understand vast arrays of data associated with climate impacts analysis of hydrologic change, assisting planners to rapidly assess potential risks associated with extreme events.

Plain Language Summary

Our study uses machine learning to characterize multiple sub-watersheds within the Colorado River Basin (CRB), based on the simulated future behavior of several drought indicators. By doing so, we are able to identify sub-watersheds of similar behavior within the CRB based on their response to climate changes and drought. We use the results from models of climate and water to estimate how drought will change in the future. We then group the behavior of sub-watersheds based on identified similarities in their response to changes we observed. We show that areas of the upper CRB could experience a large reduction in available water for evapotranspiration (for use by trees, for example), and that future hydrologic conditions may more closely resemble those of the Southwest CRB regions today. We are also able to pinpoint which sub-watersheds should expect large losses in snowpack based on simulated changes to spring streamflow. The work is important in that it highlights a key tool that can be used for rapid assessment of vast arrays of climate and hydrology data in a region that may be critically impacted by future changes in extreme events, such as drought.

1 Introduction

Drought causes tremendous global economic and environmental losses each year. However, drought is also a challenging natural disaster to quantify due to difficulty in understanding key drivers and a lack of consensus on a definition and method to identify drought conditions. Further, drought can be difficult to mitigate, leading to increased impacts to economy and society. Therefore, drought is arguably one of the greatest climate change related risks to stability of society and economy facing humans today.

It has been estimated that the monetary loss of drought for American farmers and businesses is $6-8 billion each year (in 2004 value, which is equivalent to today's value of $8.16-10.88 billion) ("Western Governors Association (WGA). Creating a Drought Early Warning System fo the 21st Century: The National Integrated Drought Information System," 2004), 2004). Despite its economic importance, drought is poorly understood among all other climate-induced disasters (e.g., flooding) due to (1) a lack of unanimous definition for drought among scientists and stakeholders (Blauhut, 2020) and (2) the complex set of factors that influence drought and its effects on society (Wilhite, 2009). Drought is often defined categorically as hydrologic (low supply of surface and sub-surface water), meteorological (low rainfall, high evapotranspiration), or agricultural (low water availability for plants). The drivers of drought are even more numerous (Xiao et al., 2018). While the implications for drought in a changing climate are not fully understood and projections of future precipitation remain uncertain, climate change is expected to amplify and intensify the hydrologic, meteorologic, and climatic factors that induce drought events leading to higher intensity and frequency of drought events in the future, with consequences for ecology, economy, and society (Zhou et al., 2019).

The Colorado River Basin (CRB) constitutes an area of increasing drought risk (Strzepek et al., 2010) and an area of high economic importance related to its freshwater resources (Bennett et al., 2021; James et al., 2014). Additionally, there is a broad diversity in ecological, climatic, and hydrologic conditions within the CRB contrasted by the arid Southwest U.S. and the high-elevation snow-dominant mountains of Colorado, Utah, and Wyoming through which the Colorado River flows. Changes in future climate within the CRB are especially concerning due to the CRB's reliance on high-elevation snowpack for annual runoff, with approximately ~70% of runoff generated from snowpack (Christensen et al., 2004). Observed snowpack has been declining historically (Fassnacht & Hultstrand, 2015), and is projected to decline strongly into the future (Ray et al., 2008).

Climate change impacts on surface water vary along elevational and thermal gradients, e.g., high elevation areas can experience greater warming and may start to behave similarly to adjacent low elevation areas. This altitudinal gradient shift has been observed among plant and animal species (Bender et al., 2019; Sekercioglu et al., 2008), snow-pack distribution (López-Moreno et al., 2009), and other hydrologic and meteorologic conditions (Beniston et al., 2018; Chang & Jung, 2010). While some climate change impacts occur gradually across these gradients, threshold (anomalous) changes may cause drastic, abrupt, shifts to watershed behavior, and key altitudinal ranges may be more sensitive than others (Ali et al., 2015; Tromp-van Meerveld & McDonnell, 2006). The most prominent example of such a threshold change to watershed hydrology is the loss of winter snowpack, which impacts the timing and volume of peak streamflow during the spring melting period (Christensen et al., 2004; Milly & Dunne, 2020; Wi et al., 2012). In this work, we attempt to identify the most sensitive areas within the

CRB to changes in drought-indicator behavior due to climate change, as well as the timing of those changes in the annual cycle, with an emphasis on threshold changes in behavior.

To address the complex relationships between climate and drought, as well as the spatial diversity and abundance of influencing factors within the CRB (Kao & Govindaraju, 2007), we present and apply a novel non-negative matrix factorization unsupervised machine learning methodology to identify changes and differences in the annual temporal behavior of various extreme drought indicators. We developed the drought indicators using historical and projected future simulations of hydrologic and water balance parameters using the Variable Infiltration Capacity (VIC) hydrology model (Liang et al., 1996). We consider five different drought indicators: the number of dry dates (*dryd*), maximum temperature (*tempx*), minimum soil moisture (*soilmn*), minimum streamflow (*qn*), and maximum evapotranspiration (*evapx*).

Machine learning has been effectively been utilized in recent years to estimate a plethora of earth science phenomena (Adhikari et al., 2020; Cho et al., 2020; Rundle et al., 2021; Yang et al., 2021). By performing these ML analyses, we can identify spatial patterns as well as threshold changes in hydrologic behavior across the CRB. Using machine learning (ML) models to isolate specific drought-indicator behaviors, we can limit our analysis of the observed indicator behavior to key seasonal periods and sub-watersheds within the CRB. ML allow us to disentangle the complex spatial and temporal relationships between drought-indicators and their influencing factors. Through use of a novel machine learning approach, we demonstrate a capability to automatically isolate where key indicator behavior contributes to drought and where and how behavior will change in the future. Using ML, we also reduce the size of the output data to analyze by separating relevant behaviors to quickly process large hydrologic model outputs (30 GB for each ESM over a 30-year time period), identify possible errors, and target unforeseen responses. This approach allows us to dramatically narrow our analysis and processing of the hydrologic model outputs, improving our ability to understand the spatial and temporal behavior of drought indicators.

This paper is organized as follows. In the Materials and Methods section, we describe the study site and the methods and data used for hydrologic modeling the hydrology of the CRB under different climatic scenarios. We describe the drought indicators chosen and how they are calculated, based on the outputs from the hydrologic modeling. We further describe the NMFk algorithm, a novel unsupervised machine learning method applied to cluster the sub-watersheds within the CRB based on their annual signal behavior. In Results, we detail ML outputs related to the clustering of drought indicators both spatially and temporally. We interpret the ML results in Discussion, including the causes and implications for drought in the CRB. The Conclusion contains a brief description of the key findings as well as a description of the utility of the ML algorithm for interpretation of model results.

2 Materials and Methods

2.1 Study Site

The study area for this research is the CRB. Located in the Southwestern Unites States and Norther Mexico, the CRB covers an area of 6.4×10^5 km^2 (Figure 1). The basin stretches from sea level in the Gulf of California, to higher than 4000 m in the Southern Rocky Mountains. The CRB contains a broad range of climate zones and ecosystems, with the observed annual average temperature ranging from 4-24 ºC and the average annual precipitation ranging from 79-1699 mm (Livneh et al., 2015). Much of the precipitation throughout the basin falls as snow at high elevations, and 70% of the annual streamflow originates in the Upper CRB upstream from Glen Canyon, Arizona (Christensen et al., 2004). Due to this fact, the CRB is often characterized in two portions: the high-elevation snow dominant Upper CRB and arid low-elevation Lower CRB. The water resources of the CRB are critical to water security within the CRB and to many population centers outside the watershed boundaries where a significant amount of the CRB water is diverted (i.e., Los Angeles, San Diego, Salt Lake City, Albuquerque, Denver, Figure 1).

2.2 Earth System Model Simulations

In this study, we use six different, commonly-used Earth System Models (ESMs) run with dynamic vegetation. The ESMs and their dynamic vegetation models are: HadGEM2-ES365 (Collins et al., 2011; Cox, 2001), MIROC-ESM (Sato et al., 2007; Watanabe et al., 2011), MPI-ESM-LR, IPSL-CM5A-LR (Dufresne et al., 2013; Krinner et al., 2005), and GFDL-ESM2M, and GFDL-ESM2G (Delworth et al., 2006; Shevliakova et al., 2009). We used statistically downscaled data from the Multivariate Adaptive Constructed Analogue (MACA) database (Abatzoglou & Brown, 2012).

For this work, we examine the representative concentration pathway (RCP) 8.5 emissions scenario, which follows shifting greenhouse gas (GHG) emissions levels over time (Le Quéré et al., 2015) and anticipates substantial increases in GHG emissions by 2100 (van Vuuren et al., 2011). The six ESMs were chosen to represent the spread of projected change in precipitation and temperature for the CRB as calculated by ESMs available in the downscaled MACA dataset used in the fifth version of the Coupled Model Intercomparison Project (CMIP5). The six selected ESMs were selected to capture the spread of scenarios from dry to wet and from the lowest to the highest temperature increase, both annually and seasonally.

2.3 Hydrologic Modeling & Drought Indicators

The ESM projected precipitation and temperature were used to force the Variable Infiltration Capacity (VIC) hydrology model (Liang et al., 1996) using different climate scenarios for historical (1970-1999) and future (2070-2099) time periods periods. The output from VIC captures the historical and future climate conditions (as physical indicators) for flow and drought conditions within the CRB. VIC was implemented and run as described in Bennett et al. (2018, 2019), and is thus only briefly described herein. VIC is a spatially distributed, macroscale hydrologic model simulating the full water and energy balance while accounting for 1-D variably saturated infiltration through the vadose zone. VIC includes a decoupled routing model that is used to estimate surface water discharge (D. Lohmann et al., 1998; Dag Lohmann et al., 1996). We executed VIC at a daily temporal and a $1/16°$ latitude/longitude (~7 km) spatial resolutions across the CRB. Simulated streamflow was calibrated by adjusting snow albedo and soil parameters across all 134 HUC8 sub-watersheds within the CRB. The calibration uses the United States Geological Survey (USGS) naturalized gauged monthly streamflow data (USBR, 2012) to compare against simulated streamflow and then uses an automated calibration tool (Yapo et al., 1998) to correct modeled biases against the USBR data (Bennett et al., 2018).

Using the hydrologic and meteorological output from the VIC model, we calculated five individual drought indicators: number of dry dates (*dryd*), maximum temperature (*tempx*), minimum soil moisture (*soilmn*), minimum streamflow (*qn*), and maximum evapotranspiration (*evapx*). As a first step, we calculate all drought indicators for the 134 HUC8 sub-watersheds for 5-day periods (73 each year, with leap year days removed, for example, January 1st-5th , 6th-10th, and so on) over the historical and future 30-year periods. We then average the 5-day-periods over the appropriate 30-year period giving us the average annual cycle for each time period at a 5-day resolution. The "delta" case is simply the averaged historical annual cycle for a drought indicator subtracted from the averaged future annual cycle. The *dryd* indicator is the number of days within a 5-day period with no precipitation, while the other indicators represent either the maximum or minimum daily value for each 5-day period. Streamflow here is the average non-routed contribution of both runoff and baseflow from an individual VIC model grid cell.

2.4 Machine Learning Methodology: NMFk

A novel unsupervised machine learning (ML) approach was applied in this work (Vesselinov et al., 2018). The ML methods are based on Nonnegative Matrix/Tensor Factorization (NMF/NTF) coupled with k-means clustering (NMFk/NTFk). The factorization is solved as a minimization problem, which also allows various optimization constraints (sometimes referred to as regularization terms) to be applied. In this way, the constraints provide an efficient way to add physics information in the ML process.

NMF is a Blind Source Separation (BSS) technique that has been widely applied to the automated extraction of hidden signals present in complex datasets (e.g., earth sciences, astronomy, biology) with little or no a-priori knowledge or physical modeling efforts (Jung et al., 2000; Nuzillard & Bijaoui, 2000; Sadhu et al., 2017). Perhaps the most prominent benefit of using an unsupervised ML is that any bias from past experience or subject-matter expertise is minimized (Belouchrani et al., 1997). Instead, the signals extracted are based only on the information within the data. NMF does not assume any specific statistical distribution or independence of the original data. However, NMF does impose nonnegative constraints on the estimated factorization matrices, so the extracted features are readily interpretable with relation to the original data. This is an improvement over other BSS techniques, such as Principle Component Analysis (PCA), that do not generate negative matrix elements and therefore do not provide direct interpretability of the original data (Kayano & Konishi, 2009).

The fundamental task of NMF is to decompose a data matrix X (with dimensions $n \times m$) into two non-negative matrices $W \in \ R^{n\times k} \ and \ H \in \ R^{k\times m}$ so that

$$X \ = \ W \times H$$

In our case, m is the number of sub-watersheds (134 HUC8 sub-watersheds), and n is the number of 5-day time periods throughout the year (73). Note that k is a positive integer (less than $min(m, n)$) defining the unknown number of original features (signals) hidden in the data (Lin, 2007). W is often regarded as the feature matrix (i.e., representing the unique signals or features present the original data), and H is called the mixing matrix capturing how the features are mixed at each watershed.

NMF determines W and H by minimizing the cost function O, which is a measure of discrepancy between actual data (X) and factorized reconstruction of X ($W \times H$). In this study, we use the Frobenius matrix norm during the minimization process:

$$O = \frac{1}{2}\|X - WH\|_F^2 = \frac{1}{2}\sum_{i=1}^{n}\sum_{j=1}^{m}(X_{ij} - (WH)_{ij})^2$$

Here, our goal is to identify and extract the hidden features (signals) in the drought indicators that contribute to the changes in historical and future hydroclimatic conditions. However, a significant limitation of the traditional NMF is that a priori knowledge of the number of features is required to solve the objective function, but this is often unknown in practice. Our novel method NMFk (Alexandrov & Vesselinov, 2014; Vesselinov et al., 2018) addresses this limiting using the assumption that an optimum number of features can be obtained based on the robustness and reproducibility of the NMF results. To this end, NMFk computes solutions for all possible numbers of features k ranging from 1 to d (less than min(m, n)) and then estimates the accuracy and robustness of these solution sets for different values of k. For each k value, the robustness is estimated in NMFk by performing a series of NMF runs (e.g., 1,000) with random initial guesses W and H elements. After that, the series of NMF solutions are grouped using a custom semi-supervised k-means clustering. The customization to the original algorithm is to keep the number of solutions in each cluster equal to the number of NMF runs (e.g., 1,000). The clustering is applied to measure how good a particular number of extracted features, k, is to accurately and robustly describe the original data. The optimal number of features k_{opt} is estimated automatically by the NMFk algorithm. A detailed description of NMFk can be found in Vesselinov et al., 2018 (Vesselinov et al., 2018).

Here, we use the climate and hydrologic conditions (outputs from VIC from the six ESM modeled climate scenarios) to extract temporal drought indicator signals for the 134 HUC8 CRB sub-watersheds. NMFk automatically identifies plausible solutions for the number of drought indicator signals present in the analyzed dataset with the optimal number of features estimated by the solution robustness. The data capture annual temporal signal from 134 HUC8 sub-watersheds resulting in a 134 x 73 matrix. The extracted drought indicator signals are defined as columns in the feature matrix, W. The estimated mixing matrix, H, represents how each of the common drought indicator signals is represented in each sub-watershed. Then, the sub-watersheds are grouped based on the dominance of extracted drought indicator signals within each sub-watershed.

We apply NMFk to historical (1970-1999) and future (2070-2099) time periods as well as the difference between the two periods (referred to as “delta”). Our unsupervised ML analyses allow us to identify the temporally unique drought indicator signals observed throughout the study region for different ESM modeled climate projecetions. Then we apply theoretical and site knowledge to relate the extracted signals to physiographical characteristics, which allows us to clarify the contributing factors to the low flow and drought events in CRB. This workflow is shown in Figure 2, which illustrates the clustering process for *qn*.

3 Results

The change in temperature and precipitation across the CRB for the complete set of 14 ESMs in the MACA database is shown in Figure 3. The mean temperature increase of the 14 ESM's is approximately $5.6 \pm\ 1.1°C$. The mean precipitation also increase by has large variance among the models ($\overline{\Delta P} = 4.5\ \pm 11.1$ %). Three of the selected ESM's used in the analysis project decreased annual precipitation (IPSL-CM5A-LR, -15.6%; MPI-ESM-LR, -3.33%; HadGEM2-ES365, -4.04%), while the other three project increased annual precipitation (GFDL-ESM2M, +1.38%; MIROC-ESM, +7.79%; GFDL-ESM2G, + 8.51%). The mean changes in annual precipitation and temperature are shown in Table 1 for each of the six models.

For brevity, we focus our presentation of results on the wettest and driest models assessed (GFDL-ESM2G and IPSL-CM5A-LR, respectively), and these models are highlighted in Figure 3. GFDL-ESM2G also exhibits significantly less warming (+$4.56°C$) than IPSL-CM5A-LR (+$6.33°C$), providing us with a warm and wet scenario (GFDL-ESM2G, referred to herein as warm/wet scenario) and a hot and dry scenario (IPSL-CM5A-LR, referred to herein as hot/dry scenario). Results for other ESMs at 3 signals can be found in the supplementary materials and will be mentioned in the text where the results of ESMs showed similar or dissimilar behavior. GFDL-ESM2G is labelled Wet, and IPSL-CM5A-LR is labelled as Dry in figures.

3.1 Maximum Temperature (*tempx*)

The spatial clustering of maximum temperature (*tempx*) for 2, 3, and 4 signals and each warm/wet and hot/dry scenario is shown in Figure 4. The rows in Figure 4 show the NMFk model results at differing number of signals (2, 3,or 4 signals), while each of the columns show the results of a particular climate scenario and time period (hot/dry, or warm/wet scenario, Historical/Future/Delta). With 2 signals (panel a1-a6), the sub-watersheds sort into the high-elevation Upper CRB and the low-elevation Lower CRB for both future and historical periods. The NMFk solution at 2 signals are able to consistently produce solutions across differing climate scenarios. The extracted 2 *tempx* signals consistently separates into the Upper and Lower CRB, with only a few solutions of NMFk found beyond 2 signals (panel b4, b6, c6). Nevertheless, the spatial clustering based on extracted *tempx* features for higher number of signals still roughly follow similar latitudinal and elevational gradients as in the 2 signal solution. For the case of 3 NMFk signals, the sub-watersheds sort into northern, central, and southern clusters (b4, b6), with the southern cluster being split in two in the case of 4 extracted signals (c6).

Figure 5 shows the temporal signal separation in *tempx* for the warm/wet and hot/dry scenarios. There is a clear separation in the temporal pattern in *tempx* between the Upper and the Lower CRB clusters for the case of 2 signals. For both historical and future periods, the Upper CRB exhibits cooler temperatures, as expected. The separation between signals is consistent throughout the year, with slightly more separation during the winter months (panels a1, a2). However, the clustering based on *tempx* extracted signals varies across the models, exhibiting large differences between panels a3 and d3 of Figures 5. The warm/wet scenario show a larger separation between signals, primarily in the spring, while the hot/dry scenario shows relatively little separation between signals, except for a brief period in June. Also, the hot/dry scenario shows the greatest discrepancy in the summer when compared to the warm/wet scenario. However, seasonal tempx differenes in the "delta" period vary across ESM's as can be seen the supplementary materials and do not appear to have a clear relationship with the projected change in precipitation.

3.2 Dry Dates (*dryd*)

The spatial clustering of *dryd* at 2 signals shows a distinct grouping in the southeast of the CRB, with the remainder of the CRB clustering together (Figure 6, panels a1-a4). This grouping grows slightly from historical to future and largely remains intact with increasing numbers of signals. At higher signals, we see less convergence and less agreement in groupings across models and time periods (Figure 6, panels b1-c6). However, the southeast grouping is represented across different scenarios and time periods, while the clustering of the remainder of the CRB sub-watersheds is more varied.

Looking at the temporal pattern for 2 signals (Figure 7, panels a1-a3,d1-d3), it is evident that the grouping of the southeast portion of the watershed is characteristic of fewer *dryd* during the summer months, for both historical and future. At a higher number of signals in the historical and future periods (panel b1,e1, f1-f2), the temporal signal separation between signal magnitude is more evident in the spring and fall as well. Still, the strength of the summer seasonality in *dryd* remains a determining factor in the clustering of sub-watersheds, especially for the cluster in the southeast basin (blue).

The difference between the historic and future conditions, “delta”, in the number of dry days (*dryd*) tends to again cluster along the Upper and Lower CRB at 2 signals across all climate scenarios, the temporal signal of these groupings tends to be quite different between the scenarios. The warm/wet scenario shows the Upper CRB as mostly experiencing fewer *dryd* throughout the year, and the Lower CRB experiences more *dryd* in the spring and fewer in the summer. The warm/wet scenario shows that both Upper and Lower CRB experience mostly more *dryd* throughout the year with some variability. It also shows a distinct increase in *dryd* in the Lower CRB for the month of July.

3.3 Maximum Evapotranspiration (*evapx*)

The spatial results for *evapx*, shown in Figure 8, again exhibit a separation between Upper CRB and Lower CRB at 2 signals (panels c1-c6), although more watersheds tend to fall into the Lower CRB grouping compared to *tempx* and *dryd*. We also see that a few watersheds in the Lower CRB geographically are grouped in the Upper basin under the historical *evapx* time period but group with the Lower basin under future periods. While we see similar spatial clustering between scenarios for the historical and future periods for 2 signals (panels a1-a2), the patterns diverge dramatically for the delta for 2 signals. The hot/dry scenario groups a large portion of the Southwest CRB along with the Upper CRB (Figure 8; panel a5), while the warm/wet scenario shows a delineation between clusters further to the north and running roughly east-west (panel a6). At 3 or more signals, *evapx* again shows a similar spatial cluster across scnearios in the historical but diverges under the future time period (Figures 8; panels b1-c6). Further, the spatial clusters become less contiguous, in some, but not all, cases (panels b4-b5, c3).

The temporal signals of *evapx*, exhibited in Figure 9, show a clear pattern. At 2 signals (Figure 9; panels a1-a2, d1-d2), the Upper CRB exhibits a peak in evapotranspiration in the summer and a minimum in evapotranspiration in the winter, while the Lower CRB grouping shows a peak in evapotranspiration in both March and a larger peak in the late summer months with a dip in evapotranspiration during May and June. At 3 or more signals (panels b1-b2, c1-c2, e1-e2, f1-f2) we see that the separation in temporal signals is largely determined by whether the signal has one peak in the early summer, or two peaks in the spring and late summer. Further, clustering is determined by the intensity of the second peak in the late summer and fall.

The scenario results show large disagreement in whether *evapx* is decreasing or increasing, particularly in the summer (Figure 9, panels a3,d3) when the discrepancy in temperature is greatest. The hot/dry scenario shows that *evapx* is decreasing across the entire basin, especially during the summer months. Further, the future hot/dry scenario shows the Upper CRB exhibiting the same summer dip in *evapx* as the Lower CRB. The warm/wet scenario shows increasing *evapx* in the Upper CRB throughout the year and increasing *evapx* across the entire CRB during July. In the warm/wet scenario, the cluster in the Upper CRB which exhibits a single peak early in the summer is consistent between historical and future time periods, both spatially and temporally.

3.4 Minimum Soil Moisture (*soilmn*)

The spatial clustering of *soilmn*, shown in Figure 10, forms the least contiguous groupings of any of drought indices. At 3 signals, sub-watersheds within a single group (red) are scattered throughout the CRB. Further, no NMFk solutions for any scenario or time period converge beyond 3 signals. When evaluating the delta in *soilmn*, it appears that differences between clusters are more localized and that local topography plays a major role in the spatial clustering. Further, at 3 signals, a small band of sub-watersheds is grouped at the center of the Lower CRB (blue at 3 signals; panels b4-b6), while many of the highest elevation sub-watersheds in the northeast of the CRB tend to group together.

The temporal signal for *soilmn*, shown in Figure 12, similarly shows a wide range of behavior and a large range in *soilmn* magnitudes. In both historical and future periods, the temporal pattern shows a grouping of sub-watersheds with little to zero *soilmn* and little *soilmn* seasonality. Other sub-watersheds show a spring peak in soil moisture, but exhibit a large range of magnitude in *soilmn* for those sub-watersheds. Looking at the delta for *soilmn*, we see that the spring peak is shifting earlier in the year and becoming larger. The grouping mentioned previously as a band of sub-watersheds across the lower CRB is largely losing *soilmn* when assessed in Figure 12 (panels a3,b3,e3, f3). The signals and seasonality of *soilmn* clusters between climate scenarios are quite similar, although the models disagree on the magnitude of *soilmn* and the magnitude of the seasonality. The hot/dry scenario exhibits a decrease in soil moisture across the CRB and a smaller peak in spring soil moisture in the future, while the warm/wet scenario shows mostly increasing soil moisture throughout the year and a similar magnitude in spring *soilmn* peak from historical to future.

3.5 Minimum Streamflow (*qn*)

The spatial clustering of *qn* shows a clear separation in Figures 13 (panels a1-b6) between the highest elevation and mountainous sub-watersheds within the CRB and the lower elevation sub-watersheds. At four signals (panels c1-c6), the clustering further splits the lower elevation and downstream sub-watersheds such that we begin to see sub-watersheds of the larger Green River valley grouped together (red; panels a1, a2, and a4) and a southeastern portion of the CRB grouped together (blue). From historical to future, the clusters of the Lower CRB begin to expand into the Upper CRB clusters. The delta panels show similar clustering to the historical and future time periods. However, the high elevation clusters tend to be less contiguous at 3 and 4 signals, and several individual sub-watersheds in the southern portion of the CRB associate with the highest elevation sub-watersheds at 3 signals.

The temporal signals of *qn*, shown in Figures 14, exhibit separation between signals based on the strong spring seasonality between different sub-watersheds. There are clear differences between clusters based on the timing and magnitude of a spring peak in *qn*, with the largest peaks in streamflow occurring later in the spring. The sub-watersheds with the largest seasonal peak in *qn* also correspond to the high-elevation mountainous sub-watersheds seen in Figure 2. For both models, the peak in *qn* shifts earlier in the year during the future period.

The delta also shows an increase in the *qn* in the mountainous sub-watersheds during March through May, followed by a decrease during June where *qn* peaks during the historical period. At 3 or more signals, the sub-watersheds with the larger changes in *qn* tend to be those with a peak in streamflow later in the year. The warm/wet scenario shows a seasonal streamflow peak in the future equal or greater than that of the past, while the hot/dry scenario shows a much smaller streamflow peak in the future.

Overall, NMFk was able to converge on a solution for nearly all scenarios and time periods at 4 signals and some instances beyond 4 signals, suggesting that significant behavioral differences exist in the *qn* signal and the expected delta in *qn* signal.

4 Discussion

The ESM projections and VIC modeling results in the CRB show large changes to the hydrologic functioning. The ESM projections for temperature generally show similar projections across all ESMs as well as those in the supplementary materials. However, large variance in the projection of future precipitation does exist (Dai, 2006). The large variability across ESMs complicates the projection of the CRB hydrologic behavior and creates difficulties when drawing overarching conclusions related to drought. Still, the warm/wet ESM scenarios may increase drought due to snowpack loss and an increased evapotranspiration response. The ML results show a perceptible difference in streamflow timing, likely due to differences in snowpack retention in the high elevation basins of the CRB. The range of possible climate scenarios considered here, regardless of ESM model, does point to a hotter CRB with large changes in the timing and magnitude of streamflow, evapotranspiration, and soil moisture that will present challenges in managing water resources in the future.

The spatial and temporal pattern of signal separation in *dryd* clearly demonstrates the influence of the North American Monsoon (NAM) as a dominant precipitation signal in the southern CRB. The NAM is most prominent in the Southeastern CRB from late June to September, resulting in an increase in precipitation (Adams & Comrie, 1997). The results show the spatial influence of the NAM increasing in the future. However, the separation of temporal signals for *dryd* does not change significantly during the active summer monsoon season and change in summer *dryd* varies across climate scenarios. Previous studies on the modeled trajectory or observed trends in the NAM are often contradictory as to whether the NAM is intensifying or weakening (Colorado-Ruiz et al., 2018; Demaria et al., 2019; Luong et al., 2017). The ML analysis of *evapx* also shows signs of influence from the NAM. The second spike in evapotranspiration in the Lower CRB in the late summer demonstrates the water inputs provided by the NAM. Further, the ML extracted spatial patterns for the Lower CRB sub-watersheds at 3 and 4 signals appears dependent on the strength of the NAM in those areas.

The *evapx* extracted signals show a clear separation between two evaporation regimes: the water-limited Lower CRB and a more radiation-limited Upper CRB. The water-limited nature of the Lower CRB explains the bi-modal annual signal of the Lower CRB, where little water is available for evapotranspiration in the warmer pre-monsoon season months. The hot/dry scenario shows a distinct shift in the future toward an increasingly water limited regime in the summer across the entire CRB. The future hot/dry scenario shows a large dip in *evapx* across the basin in June and July when evapotranspiration decreases because of a lack of available water. Increasing evaporative demand associated with climate change is a key driver of drought in the American Southwest, with previous studies showing that increases in evaporative demand may overcome any increases in future precipitation (Ault et al., 2016; Cook et al., 2014, 2015). Our study shows increasing evaporative demand in critical sub-basins as an important driver of drought.

The 4-signal spatial clustering shows the borders between a water-limited regime and a more radiation-limited regime (purple) in *evapx*. Both hot/dry scenarios show a shift toward the water-limited regime as the Upper Basin cluster shrinks. However, there is a large difference in the extent to which the water-limited regime is growing. The hot/dry scenario shows that only the highest and wettest sub-watersheds will remain somewhat energy-limited during the summer months while the warm/wet scenario shows a larger number of sub-watersheds within the energy-limited regime.

It is clear that uncertainty in ESM precipitation could result in a wide range of drought scenarios, with the driest of those scenarios resulting in threshold changes in areas of the Upper CRB. Further, despite projected temperature exhibiting less variance across ESMs, there is still a large discrepancy in the summer *tempx* between the two scenarios shown here that could drive large changes to *evapx* during the summer months. The future hot/dry scenario clustering also shows many of the sub-watersheds within the Green River Valley near the border of Colorado, Utah, and Wyoming clustering together. The extracted temporal signal for this clustering is characterized by a large peak in *evapx* during the late spring, and a large dip in evapotranspiration in June. The results show that the Green River Valley area may experience large drought pressures from increasing aridity combined with changes in the seasonality of streamflow and snowmelt upstream. Further, previous studies have cited increasing evapotranspiration as a major risk in the reduction of Colorado River streamflow (Udall & Overpeck, 2017).

The ML results of both *soilmn* and *qn* exhibit large influences from changes in snowmelt behavior. A seasonal increase in *soilmn* and *qn* occurs concurrently during the spring snowmelt period. Spatially, *qn* separates neatly into the snow-dominated mountainous regions of the CRB and sub-watersheds with relatively little snowfall. *Soilmn*, however, does not. Instead, influences from vegetation, geology, and soil type likely complicate the soil moisture signals as we see a large difference in soil moisture magnitude in the ML results. Changes in *soilmn* seem to reflect both seasonal changes in snowmelt and larger changes in soil moisture magnitude throughout the year.

A key area of change is the collection of sub-watersheds in the mountainous region of Arizona which group together in the "delta" analysis. This region exhibits a large loss in *soilmn* throughout the year, especially when projected by the hot/dry scenario, but also for the wet scenario. This could be caused by a decrease in orographic precipitation due to drier air, combined with an increase in evapotranspiration due to an increase in vapor pressure deficit. The combined pressures of increasing vapor pressure deficit and loss of snowmelt could drive this region to experience a severe decrease in existing soil moisture, regardless of precipitation changes. The delta of *soilmn* is drastically different between climate models as the hot/dry scenario shows large decrases in *soilmn* and the warm/wet scenario exhibits large increases across nearly the entire basin. The consistency of this discrepancy suggests that differences in projected temperature contribute to large changes in soil moisture as higher temperature shift the moisture balance toward drier conditions (Ault et al., 2016).

The streamflow delta certainly indicates a significant shift in the timing of peak streamflow for the entire CRB and especially the mountainous regions. This shift in streamflow is well documented and has implications in reservoir management and water availability for irrigation (Christensen et al., 2004; Ficklin et al., 2013; Solander et al., 2017). However, the variability in projected climate scenarios results in significant variability in the magnitude of streamflow. The hot/dry scenario forecasts significantly lower *qn* values in the future, while the wet scenario forecasts little delta in *qn* magnitude while also exhibiting significant shifts in the timing of spring snowmelt runoff.

Previous studies of snowpack trends in the western U.S. have found that while large snowpack losses have been observed in mid-altitude areas, the relatively higher altitude regions have experienced little to no change in the snowpack (Bales et al., 2006; Howat & Tulaczyk, 2005). The altitudinal gradient in snow-melt loss previously resulted in large changes to the snowpack in the Sierra Nevada and Cascade Mountain ranges, with less snowpack changes in the high elevation Rocky Mountains of Colorado. However, high elevation areas of the CRB are projected to see a large loss of snowpack as temperatures continue to rise (Fyfe et al., 2017; Pederson et al., 2013; Rhoades et al., 2018). The detected threshold behavior of snowmelt in the CRB by our ML analyses is intriguing. It also demonstrates the capability of the ML algorithm in separating the changes hydrologic behavior related to climate change. ML results for 2 extracted signals clearly identify the areas of large streamflow changes due to snowmelt in the mountainous regions of the CRB. Further, at a greater number of signals, the algorithm was able to separate the mountainous regions exhibiting snowmelt into separate groups where snowmelt changes were more or less severe, delineating where differences in behavior exist based on threshold hydrologic responses to gradients of temperature change.

The applied unsupervised ML algorithm based on non-negative matrix factorization (NMFk) proved useful in separating the annual signatures of various drought indicators. The algorithm automatically detected seasonal differences in *qn*, *soilmn*, *evapx*, and *dryd* which can be explained by differences in climate, precipitation sources, and snowmelt timing. NMFk was also able to distinguish between watersheds based on the magnitude of the extracted signal as in the case of *soilmn*, *tempx*, and *evapx*. NMFk was particularly useful when applied to the delta estimates in drought indicators for the sub-watersheds representing the historic and future model outputs. NMFk was able to identify key watersheds drought indicators that are projected to change the most or experience a significant change in seasonality. However, because we are not modeling drought or using a specific drought index (Dai, 2011; Palmer, 1965) directly, it is difficult to quantify how the indicators will concurrently contribute to drought in the future. While NMFk can cluster the indicators concurrently, the interpretation of the results would require additional work in parsing the direction of change and the importance of drought indicators. Overall, we found that the NMFk algorithm is a valuable tool in identifying and interpreting the key regions, timing, and magnitude of change in drought indicators where future research and analysis can be more focused on certain processes or regions where drought pressures appear to be increasing.

5 Conclusions

Using a novel application of unsupervised machine learning based on non-negative matrix factorization, we were able to separate seasonal watershed behaviors related to drought across a large range of environmental and climatic factors. Using historical and future climate projections from ESMs, we were able to rapidly assess seasonal changes in the behavior of drought under different climate conditions. Among the most pertinent changes was the seasonality and magnitude of *qn* related to the timing and magnitude of snowmelt runoff. The ML algorithm automatically separated the sub-watersheds in the mountainous regions of the CRB into separate groups based on differences in the *qn* signal response.

While large changes in *soilmn* for some regions were observed in the results, the modeled climate scenarios showed large disagreement on whether the *soilmn* was decreasing or increasing across large areas in the CRB. Some mountainous regions of Arizona indicated a decrease in *soilmn* for both ESM scenarios; likely a result of changes in precipitation and temperature inputs, loss of snowpack, and increases in evapotranspiration demands.

Other findings included the decrease in summer *evapx* in many basins, which indicates a lack of water available for evapotranspiration in these basins. The shift toward a water-limited evaporation regime was most evident in the hot/dry scenario model (IPSL-CM5A-LR) but was also observed in some sub-watersheds in the warm/wet scenario model (GFDL-ESM2G) as well. Areas of the Green River Valley in the Upper CRB appear to be particularly vulnerable to a shift in *evapx* due to water availability. The combined effect of streamflow shifts in timing and magnitude and changes in evaporation regimes are concerning for the ability of infrastructure to provide the needed storage to accommodate surface-water demands in late summer. While large uncertainties exist in the projected precipitation within the CRB, our analysis indicates increased risk of drought and surface-water losses in the future.

The applied unsupervised machine learning methodology worked well to distinguish the temporal features of drought indicators and provided utility in change detection, feature extraction, and interpretation of modeled hydrologic and climatic features. Of particular interest, the ML algorithm was able to distinguish between different progressions of snowpack and snowmelt change, as well as threshold changes to the evaporation signal. From the ML results, we were able to identify some key drivers of change based on the spatial and temporal patterns of the clustering. From this information, we are able to extract key areas of change within the CRB to provide a more targeted analysis of the factors specific to the changes within those key areas.

While additional work is required to further examine the drivers of drought and their joint effects on the CRB, the analyses presented here demonstrate the value of the ML algorithm in change detection research related to spatiotemporal patterns in climate and hydrologic applications. The ML algorithm can provide valuable insight into the processing of 2D or 3D model output from climate or other spacetime oriented simulations that produce large datasets. Unsupervised machine learning, as shown here, can help aid in the analysis and interpretation of large-scale model outputs for a large variety of applications.

Acknowledgments, Samples, and Data

CT and KEB, were funded under the Los Alamos National Laboratory Lab Directed Research and Development (LDRD) Early Career Research Program (20180621ECR) for components of the work. Additionally, we acknowledge the initial support under LDRD DR (20150397DR), which allowed KEB to develop the VIC modeling work the analysis is based on (completed under Los Alamos Director's Postdoctoral Fellowship, 20160654PRD). We acknowledge the support of Dr. Feng Yu in early iterations of this work.

Downscaled CMIP5 climate model projections may be downloaded via the MACA web portal: https://climate.northwestknowledge.net/MACA/ (accessed on 20 October 2020). VIC model may be downloaded via GitHub: https://github.com/UW-Hydro/VIC (accessed on 20 October 2020).

Historical VIC forcing data may be obtained from ftp://gdo-dcp.ucllnl.org/pub/dcp/archive/OBS/livneh2014.1_16deg/ (accessed on 20 October 2020).

Naturalized streamflow data for the Colorado River basin may be obtained from USBR: https://www.usbr.gov/lc/region/g4000/NaturalFlow/current.html (accessed on 20 October 2020) (U.S. Bureau of Reclamation, 2018). Other model parameter files and model outputs may be obtained by contacting the authors.

The applied unsupervised machine learning based on non-negative matrix factorization (NMFk) is open source and a part of a general AI/ML framework called SmartTensors. The source code, documentation, examples, and results from other ML studies are available at https://github.com/SmartTensors.

References

Abatzoglou, J. T., & Brown, T. J. (2012). A comparison of statistical downscaling methods suited for wildfire applications. *International Journal of Climatology*, *32*(5), 772–780. https://doi.org/10.1002/joc.2312

Adams, D. K., & Comrie, A. C. (1997). The North American Monsoon. *Bulletin of the American Meteorological Society*, *78*(10), 2197–2214. https://doi.org/10.1175/1520-0477(1997)078<2197:tnam>2.0.co;2

Adhikari, A., Ehsani, M. R., Song, Y., & Behrangi, A. (2020). Comparative Assessment of Snowfall Retrieval From Microwave Humidity Sounders Using Machine Learning Methods. *Earth and Space Science*, *7*(11), e2020EA001357. https://doi.org/10.1029/2020EA001357

Alexandrov, B. S., & Vesselinov, V. V. (2014). Blind source separation for groundwater pressure analysis based on nonnegative matrix factorization. *Water Resources Research*, *50*(9), 7332–7347. https://doi.org/10.1002/2013WR015037

Ali, G., Tetzlaff, D., McDonnell, J. J., Soulsby, C., Carey, S., Laudon, H., et al. (2015). Comparison of threshold hydrologic response across northern catchments. *Hydrological Processes*, *29*(16), 3575–3591. https://doi.org/10.1002/hyp.10527

Ault, T. R., Mankin, J. S., Cook, B. I., & Smerdon, J. E. (2016). Relative impacts of mitigation, temperature, and precipitation on 21st-century megadrought risk in the American Southwest. *Science Advances*, *2*(10). https://doi.org/10.1126/SCIADV.1600873

Bales, R. C., Molotch, N. P., Painter, T. H., Dettinger, M. D., Rice, R., & Dozier, J. (2006). Mountain hydrology of the western United States. *Water Resources Research*, *42*(8). https://doi.org/10.1029/2005WR004387

Belouchrani, A., Abed-Meraim, K., Cardoso, J. F., & Moulines, E. (1997). A blind source separation technique using second-order statistics. *IEEE Transactions on Signal Processing*, *45*(2), 434–444. https://doi.org/10.1109/78.554307

Bender, I. M. A., Kissling, W. D., Böhning-Gaese, K., Hensen, I., Kühn, I., Nowak, L., et al. (2019). Projected impacts of climate change on functional diversity of frugivorous birds along a tropical elevational gradient. *Scientific Reports*, *9*(1), 53113. https://doi.org/10.1038/s41598-019-53409-6

Beniston, M., Farinotti, D., Stoffel, M., Andreassen, L. M., Coppola, E., Eckert, N., et al. (2018, March 1). The European mountain cryosphere: A review of its current state, trends, and future challenges. *Cryosphere*. Copernicus GmbH. https://doi.org/10.5194/tc-12-759-2018

Bennett, K. E., Urrego Blanco, J. R., Jonko, A., Bohn, T. J., Atchley, A. L., Urban, N. M., & Middleton, R. S. (2018). Global Sensitivity of Simulated Water Balance Indicators Under Future Climate Change in the Colorado Basin. *Water Resources Research*, *54*(1), 132–149. https://doi.org/10.1002/2017WR020471

Bennett, K. E., Talsma, C., & Boero, R. (2021). Concurrent Changes in Extreme Hydroclimate Events in the Colorado River Basin. *Water*, *13*(7), 978. https://doi.org/10.3390/w13070978

Blauhut, V. (2020, November 1). The triple complexity of drought risk analysis and its visualisation via mapping: a review across scales and sectors. *Earth-Science Reviews*. Elsevier B.V. https://doi.org/10.1016/j.earscirev.2020.103345

Chang, H., & Jung, I. W. (2010). Spatial and temporal changes in runoff caused by climate change in a complex large river basin in Oregon. *Journal of Hydrology*, *388*(3–4), 186–207. https://doi.org/10.1016/j.jhydrol.2010.04.040

Cho, D., Yoo, C., Im, J., & Cha, D.-H. (2020). Comparative Assessment of Various Machine Learning-Based Bias Correction Methods for Numerical Weather Prediction Model Forecasts of Extreme Air Temperatures in Urban Areas. *Earth and Space Science*, *7*(4), e2019EA000740. https://doi.org/10.1029/2019EA000740

Christensen, N. S., Wood, A. W., Voisin, N., Lettenmaier, D. P., & Palmer, R. N. (2004). *The Effects Of Climate Change on the Hydrology and Water Resources of the Colorado River Basin*.

Collins, W. J., Bellouin, N., Doutriaux-Boucher, M., Gedney, N., Halloran, P., Hinton, T., et al. (2011). Development and evaluation of an Earth-System model - HadGEM2. *Geoscientific Model Development*, *4*(4), 1051–1075. https://doi.org/10.5194/gmd-4-1051-2011

Colorado-Ruiz, G., Cavazos, T., Salinas, J. A., Grau, P. De, & Ayala, R. (2018). Climate change projections from Coupled Model Intercomparison Project phase 5 multi-model weighted ensembles for Mexico, the North American monsoon, and the mid-summer drought region. *International Journal of Climatology*, *38*(15), 5699–5716. https://doi.org/10.1002/JOC.5773

Cook, B. I., Smerdon, J. E., Seager, R., & Coats, S. (2014). Global warming and 21st century drying. *Climate Dynamics 2014 43:9*, *43*(9), 2607–2627. https://doi.org/10.1007/S00382-014-2075-Y

Cook, B. I., Ault, T. R., & Smerdon, J. E. (2015). Unprecedented 21st century drought risk in the American Southwest and Central Plains. *Science Advances*, *1*(1). https://doi.org/10.1126/SCIADV.1400082

Cox, P. M. (2001). *Description of the "TRIFFID" Dynamic Global Vegetation Model*. Bracknell, UK.

Dai, A. (2006). Precipitation Characteristics in Eighteen Coupled Climate Models. *Journal of Climate*, *19*(18), 4605–4630. https://doi.org/10.1175/JCLI3884.1

Dai, A. (2011). Drought under global warming: a review. *Wiley Interdisciplinary Reviews: Climate Change*, *2*(1), 45–65. https://doi.org/10.1002/WCC.81

Delworth, T. L., Broccoli, A. J., Rosati, A., Stouffer, R. J., Balaji, V., Beesley, J. A., et al. (2006). GFDL's CM2 global coupled climate models. Part I: Formulation and simulation characteristics. *Journal of Climate*, *19*(5), 643–674. https://doi.org/10.1175/JCLI3629.1

Demaria, E. M. C., Hazenberg, P., Scott, R. L., Meles, M. B., Nichols, M., & Goodrich, D. (2019). Intensification of the North American Monsoon Rainfall as Observed From a Long-Term High-Density Gauge Network. *Geophysical Research Letters*, *46*(12), 6839–6847. https://doi.org/10.1029/2019GL082461

Dufresne, J. L., Foujols, M. A., Denvil, S., Caubel, A., Marti, O., Aumont, O., et al. (2013). Climate change projections using the IPSL-CM5 Earth System Model: From CMIP3 to CMIP5. *Climate Dynamics*, *40*(9–10), 2123–2165. https://doi.org/10.1007/s00382-012-1636-1

Fassnacht, S. R., & Hultstrand, M. (2015). Snowpack variability and trends at long-term stations in Northern Colorado, USA. *IAHS-AISH Proceedings and Reports*, *371*, 131–136. https://doi.org/10.5194/piahs-371-131-2015

Ficklin, D. L., Stewart, I. T., & Maurer, E. P. (2013). Climate Change Impacts on Streamflow and Subbasin-Scale Hydrology in the Upper Colorado River Basin. *PLoS ONE*, *8*(8), e71297. https://doi.org/10.1371/journal.pone.0071297

Fyfe, J. C., Derksen, C., Mudryk, L., Flato, G. M., Santer, B. D., Swart, N. C., et al. (2017). Large near-Term projected snowpack loss over the western United States. *Nature Communications*, *8*(1), 1–7. https://doi.org/10.1038/ncomms14996

Howat, I. M., & Tulaczyk, S. (2005). Climate sensitivity of spring snowpack in the Sierra Nevada. *Journal of Geophysical Research: Earth Surface*, *110*(F4), n/a-n/a. https://doi.org/10.1029/2005JF000356

James, T., Evans, A., Madly, E., & Kelly, C. (2014). *The Economic Importance of the Colorado River To the Basin Region*.

Jung, T.-P., Makeig, S., Humphries, C., Lee, T.-W., McKeown, M. J., Iragui, V., & Sejnowski, T. J. (2000). Removing electroencephalographic artifacts by blind source separation. *Psychophysiology*, *37*(2), 163–178. https://doi.org/10.1111/1469-8986.3720163

Kao, S., & Govindaraju, R. S. (2007). A bivariate frequency analysis of extreme rainfall with implications for design. *Journal of Geophysical Research: Atmospheres*, *112*(D13), 2007JD008522. https://doi.org/10.1029/2007JD008522

Kayano, M., & Konishi, S. (2009). Functional principal component analysis via regularized Gaussian basis expansions and its application to unbalanced data. *Journal of Statistical Planning and Inference*, *139*(7), 2388–2398. https://doi.org/10.1016/j.jspi.2008.11.002

Krinner, G., Viovy, N., de Noblet-Ducoudré, N., Ogée, J., Polcher, J., Friedlingstein, P., et al. (2005, March 1). A dynamic global vegetation model for studies of the coupled atmosphere-biosphere system. *Global Biogeochemical Cycles*. John Wiley & Sons, Ltd. https://doi.org/10.1029/2003GB002199

Liang, X., Wood, E. F., & Lettenmaier, D. P. (1996). Surface soil moisture parameterization of the VIC-2L model: Evaluation and modification. *Global and Planetary Change*, *13*(1–4), 195–206. https://doi.org/10.1016/0921-8181(95)00046-1

Livneh, B., Bohn, T. J., Pierce, D. W., Munoz-Arriola, F., Nijssen, B., Vose, R., et al. (2015). A spatially comprehensive, hydrometeorological data set for Mexico, the U.S., and Southern Canada 1950-2013. *Scientific Data*, *2*(1), 1–12. https://doi.org/10.1038/sdata.2015.42

Lohmann, D., Raschke, E., Nijssen, B., & Lettenmaier, D. P. (1998). Hydrologie à l'échelle régionale: I. Formulation du modèle VIC-2L couplé à un modèle du transfert de l'eau. *Hydrological Sciences Journal*, *43*(1), 131–141. https://doi.org/10.1080/02626669809492107

Lohmann, Dag, Nolte-Holube, R., & Raschke, E. (1996). A large-scale horizontal routing model to be coupled to land surface parametrization schemes. *Tellus A*, *48*(5), 708–721. https://doi.org/10.1034/j.1600-0870.1996.t01-3-00009.x

López-Moreno, J. I., Goyette, S., & Beniston, M. (2009). Impact of climate change on snowpack in the Pyrenees: Horizontal spatial variability and vertical gradients. *Journal of Hydrology*, *374*(3–4), 384–396. https://doi.org/10.1016/j.jhydrol.2009.06.049

Luong, T. M., Castro, C. L., Chang, H.-I., Lahmers, T., Adams, D. K., & Ochoa-Moya, C. A. (2017). The More Extreme Nature of North American Monsoon Precipitation in the Southwestern United States as Revealed by a Historical Climatology of Simulated Severe Weather Events. *Journal of Applied Meteorology and Climatology*, *56*(9), 2509–2529. https://doi.org/10.1175/JAMC-D-16-0358.1

Milly, P. C. D., & Dunne, K. A. (2020). *Colorado River flow dwindles as warming-driven loss of reflective snow energizes evaporation Downloaded from*.

Nuzillard, D., & Bijaoui, A. (2000). Blind source separation and analysis of multispectral astronomical images. *Astronomy and Astrophysics Supplement Series*, *147*(1), 129–138. https://doi.org/10.1051/aas:2000292

Palmer, W. C. (1965). *Meteorological Drought*. Washington DC: U.S. Weather Bureau.

Pederson, G. T., Betancourt, J. L., & McCabe, G. J. (2013). Regional patterns and proximal causes of the recent snowpack decline in the Rocky Mountains, U.S. *Geophysical Research Letters*, *40*(9), 1811–1816. https://doi.org/10.1002/grl.50424

Le Quéré, C., Moriarty, R., Andrew, R. M., Canadell, J. G., Sitch, S., Korsbakken, J. I., et al. (2015). Earth System Science Data. *Global Carbon Budget*, *7*(2), 349–396. https://doi.org/10.5194/essd-7-349-2015

Ray, A., Barsugli, J., & Averyt, K. (2008). Climate change in Colorado: a synthesis to support water resources management and adaptation. *The Colorado Water Conservation Board*, (September 2008), 1–58.

Rhoades, A. M., Ullrich, P. A., & Zarzycki, C. M. (2018). Projecting 21st century snowpack trends in western USA mountains using variable-resolution CESM. *Climate Dynamics*, *50*(1–2), 261–288. https://doi.org/10.1007/s00382-017-3606-0

Rundle, J. B., Donnellan, A., Fox, G., Crutchfield, J. P., & Granat, R. (2021). Nowcasting Earthquakes:Imaging the Earthquake Cycle in California with Machine Learning. *Earth and Space Science*, *n/a*(n/a), e2021EA001757. https://doi.org/10.1029/2021EA001757

Sadhu, A., Narasimhan, S., & Antoni, J. (2017, September 15). A review of output-only structural mode identification literature employing blind source separation methods. *Mechanical Systems and Signal Processing*. Academic Press. https://doi.org/10.1016/j.ymssp.2017.03.001

Sato, H., Itoh, A., & Kohyama, T. (2007). SEIB-DGVM: A new Dynamic Global Vegetation Model using a spatially explicit individual-based approach. *Ecological Modelling*, *200*(3–4), 279–307. https://doi.org/10.1016/j.ecolmodel.2006.09.006

Sekercioglu, C. H., Schneider, S. H., Fay, J. P., & Loarie, S. R. (2008). Climate Change, Elevational Range Shifts, and Bird Extinctions. *Conservation Biology*, *22*(1), 140–150. https://doi.org/10.1111/j.1523-1739.2007.00852.x

Shevliakova, E., Pacala, S. W., Malyshev, S., Hurtt, G. C., Milly, P. C. D., Caspersen, J. P., et al. (2009). Carbon cycling under 300 years of land use change: importance of the secondary vegetation sink. *Global Biogeochemical Cycles*, *23*(2). https://doi.org/10.1029/2007GB003176

Solander, K. C., Bennett, K. E., & Middleton, R. S. (2017). Shifts in historical streamflow extremes in the Colorado River Basin. *Journal of Hydrology: Regional Studies*, *12*, 363–377. https://doi.org/10.1016/j.ejrh.2017.05.004

Strzepek, K., Yohe, G., Neumann, J., & Boehlert, B. (2010). Characterizing changes in drought risk for the United States from climate change. *Environmental Research Letters*, *5*(4), 044012. https://doi.org/10.1088/1748-9326/5/4/044012

Tromp-van Meerveld, H. J., & McDonnell, J. J. (2006). Threshold relations in subsurface stormflow: 1. A 147-storm analysis of the Panola hillslope. *Water Resources Research*, *42*(2), 2410. https://doi.org/10.1029/2004WR003778

Udall, B., & Overpeck, J. (2017). The twenty-first century Colorado River hot drought and implications for the future. *Water Resources Research*, *53*(3), 2404–2418. https://doi.org/10.1002/2016WR019638

USBR. (2012). *Colorado River Basin Water Supply and Demand Study. Tech. Rep. B.* Boulder City, Nevadea.

Vesselinov, V. V., Alexandrov, B. S., & O'Malley, D. (2018). Contaminant source identification using semi-supervised machine learning. *Journal of Contaminant Hydrology*, *212*, 134–142. https://doi.org/10.1016/j.jconhyd.2017.11.002

van Vuuren, D. P., Edmonds, J., Kainuma, M., Riahi, K., Thomson, A., Hibbard, K., et al. (2011). The representative concentration pathways: An overview. *Climatic Change*, *109*(1), 5–31. https://doi.org/10.1007/s10584-011-0148-z

Watanabe, S., Hajima, T., Sudo, K., Nagashima, T., Takemura, T., Okajima, H., et al. (2011). MIROC-ESM 2010: Model description and basic results of CMIP5-20c3m experiments. *Geoscientific Model Development*, *4*(4), 845–872. https://doi.org/10.5194/gmd-4-845-2011

Western Governors Association (WGA). Creating a Drought Early Warning System fo the 21st Century: The National Integrated Drought Information System. (2004).

Wi, S., Dominguez, F., Durcik, M., Valdes, J., Diaz, H. F., & Castro, C. L. (2012). Climate change projection of snowfall in the Colorado River Basin using dynamical downscaling. *Water Resources Research*, *48*(5). https://doi.org/10.1029/2011WR010674

Wilhite, D. A. (2009). Drought monitoring as a component of drought preparedness planning. In *Advances in Natural and Technological Hazards Research* (Vol. 26, pp. 3–19). Springer Netherlands. https://doi.org/10.1007/978-1-4020-9045-5_1

Xiao, M., Udall, B., & Lettenmaier, D. P. (2018). On the Causes of Declining Colorado River Streamflows. *Water Resources Research*, *54*(9), 6739–6756. https://doi.org/10.1029/2018WR023153

Yang, Y., Anderson, A., Kiv, D., Germann, J., Fuchs, M., Palm, S., & Wang, T. (2021). Study of Antarctic Blowing Snow Storms Using MODIS and CALIOP Observations With a Machine Learning Model. *Earth and Space Science*, *8*(1), e2020EA001310. https://doi.org/10.1029/2020EA001310

Yapo, P. O., Gupta, H. V., & Sorooshian, S. (1998). Multi-objective global optimization for hydrologic models. *Journal of Hydrology*, *204*(1–4), 83–97. https://doi.org/10.1016/S0022-1694(97)00107-8

Zhou, S., Zhang, Y., Williams, A. P., & Gentine, P. (2019). Projected increases in intensity, frequency, and terrestrial carbon costs of compound drought and aridity events. *Science Advances*, *5*(1), eaau5740. https://doi.org/10.1126/sciadv.aau5740

Supplementary Materials: Characterizing Drought Behavior using Unsupervised Machine Learning for Improved Understanding of Future Drought in the Colorado River Basin

Carl J. Talsma[1], Katrina E. Bennett[1], Velimir V. Vesselinov[1]

[1] Earth and Environmental Sciences, Los Alamos National Laboratory, Los Alamos, NM, 87545.

Corresponding authors: Carl J. Talsma(talsmac83@lanl.gov), Velimir V. Vesselinov (vvv@lanl.gov)

S1: Spatial results of historical NMFk clustering algorithm of each drought indicator for each of six ESMs at 3 signals and ordered from driest (left) to wettest (right) future projection.

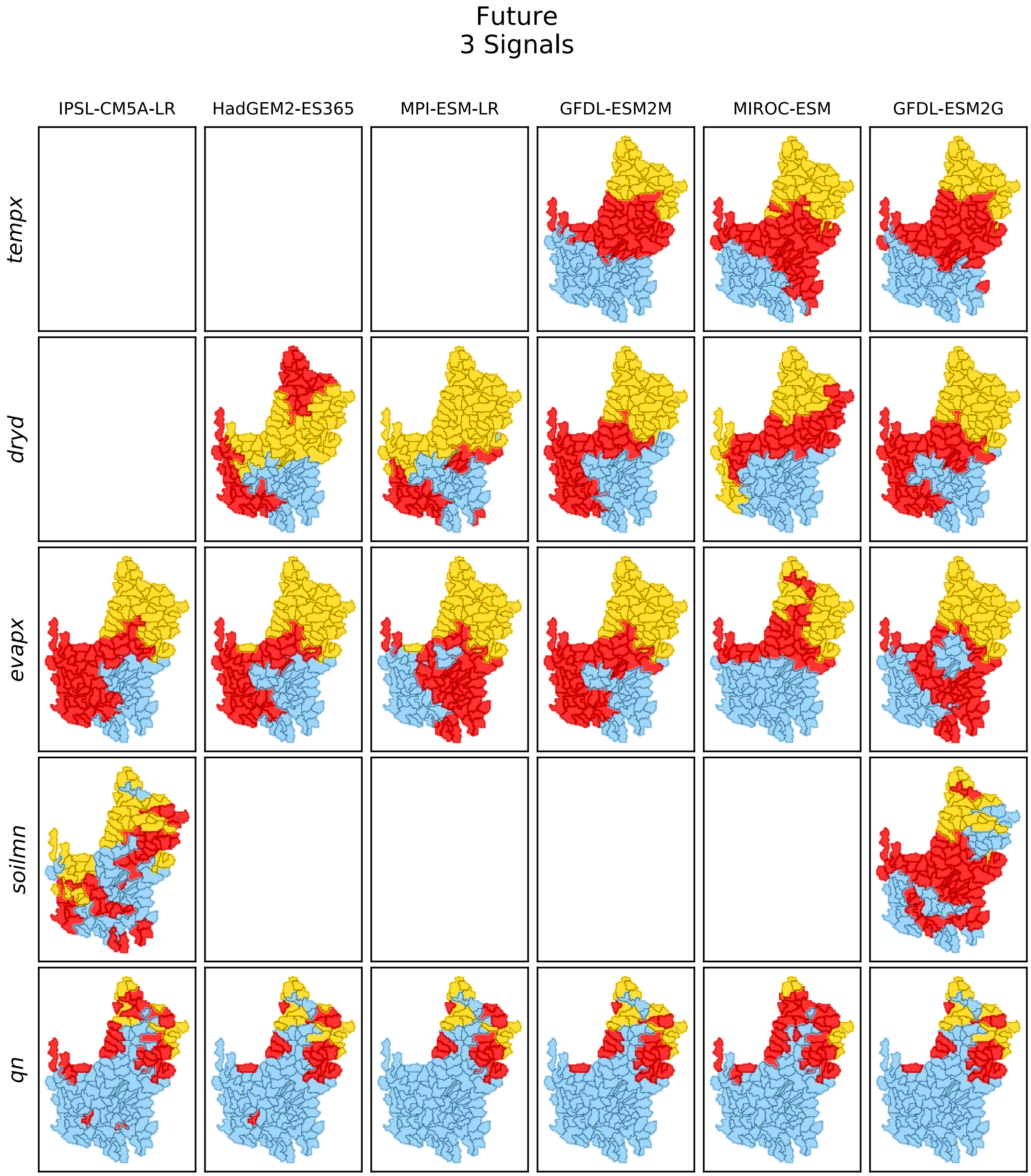

S2: Spatial results of future NMFk clustering algorithm of each drought indicator for each of six ESMs at 3 signals and ordered from driest (left) to wettest (right) future projection.

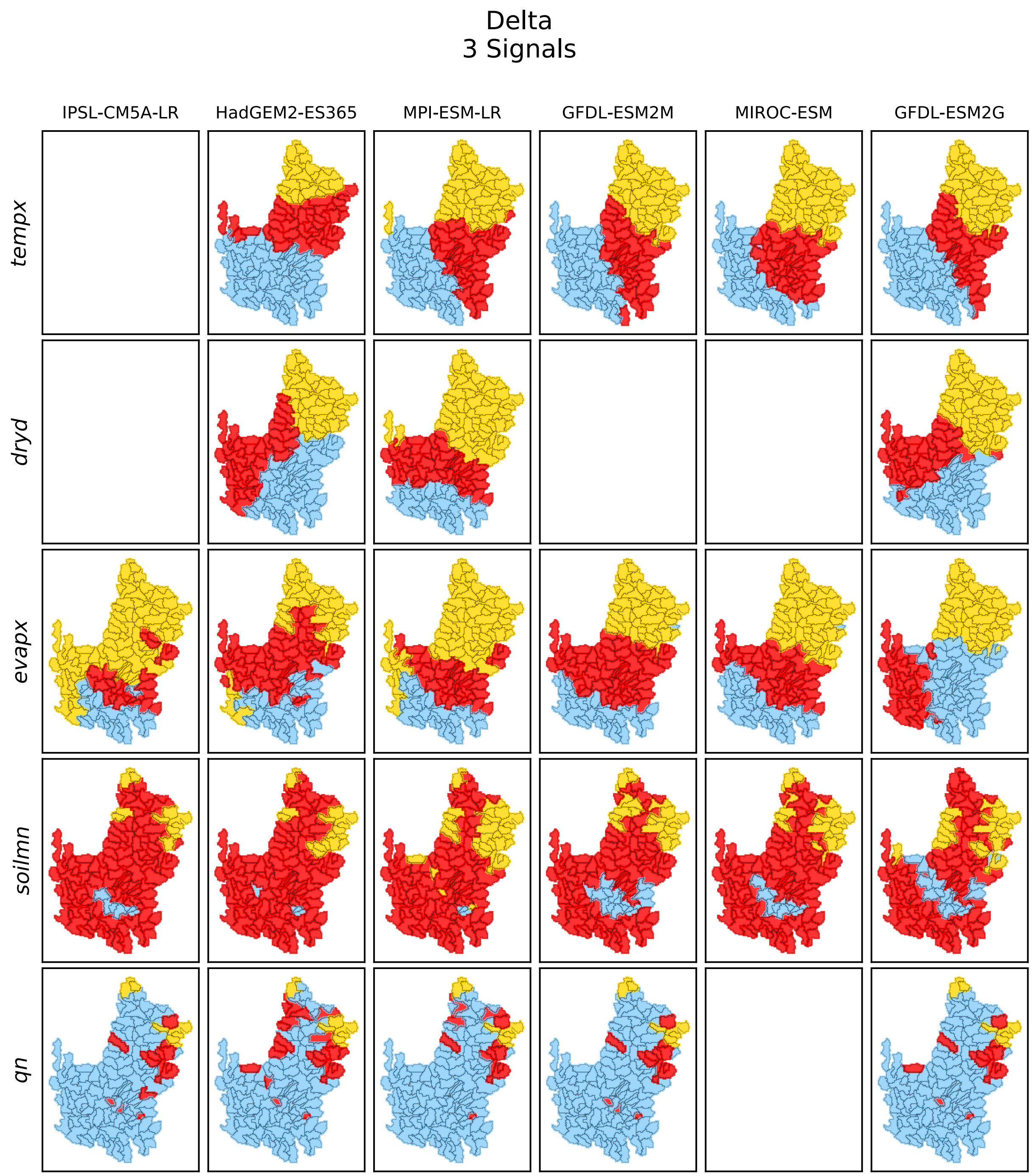

S3: Spatial results of the 'delta' NMFk clustering algorithm of each drought indicator for each of six ESMs at 3 signals and ordered from driest (left) to wettest (right) future projection.

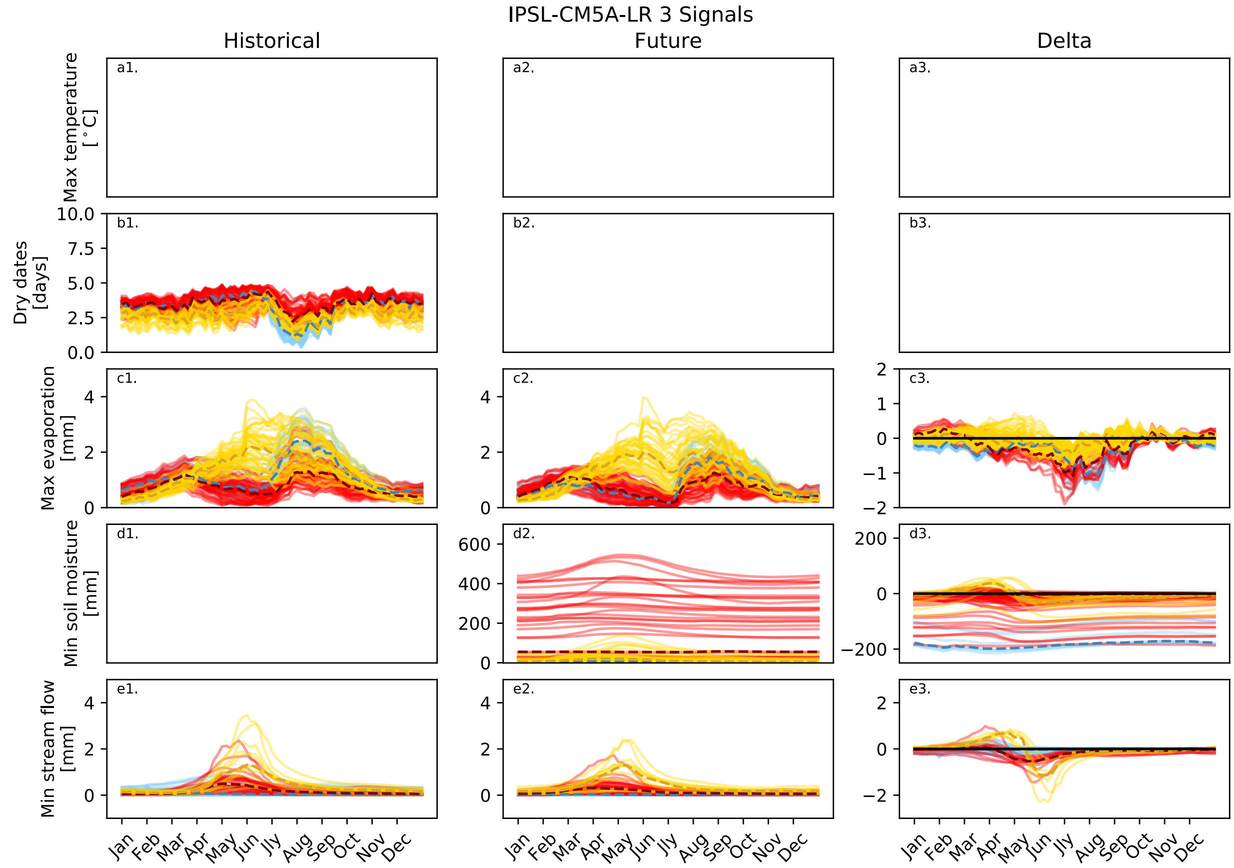

S4: Temporal results of the NMFk clustering at 3 signals for the IPSL-CM5A-LR model for each time period and the ‘delta’ between historical and future.

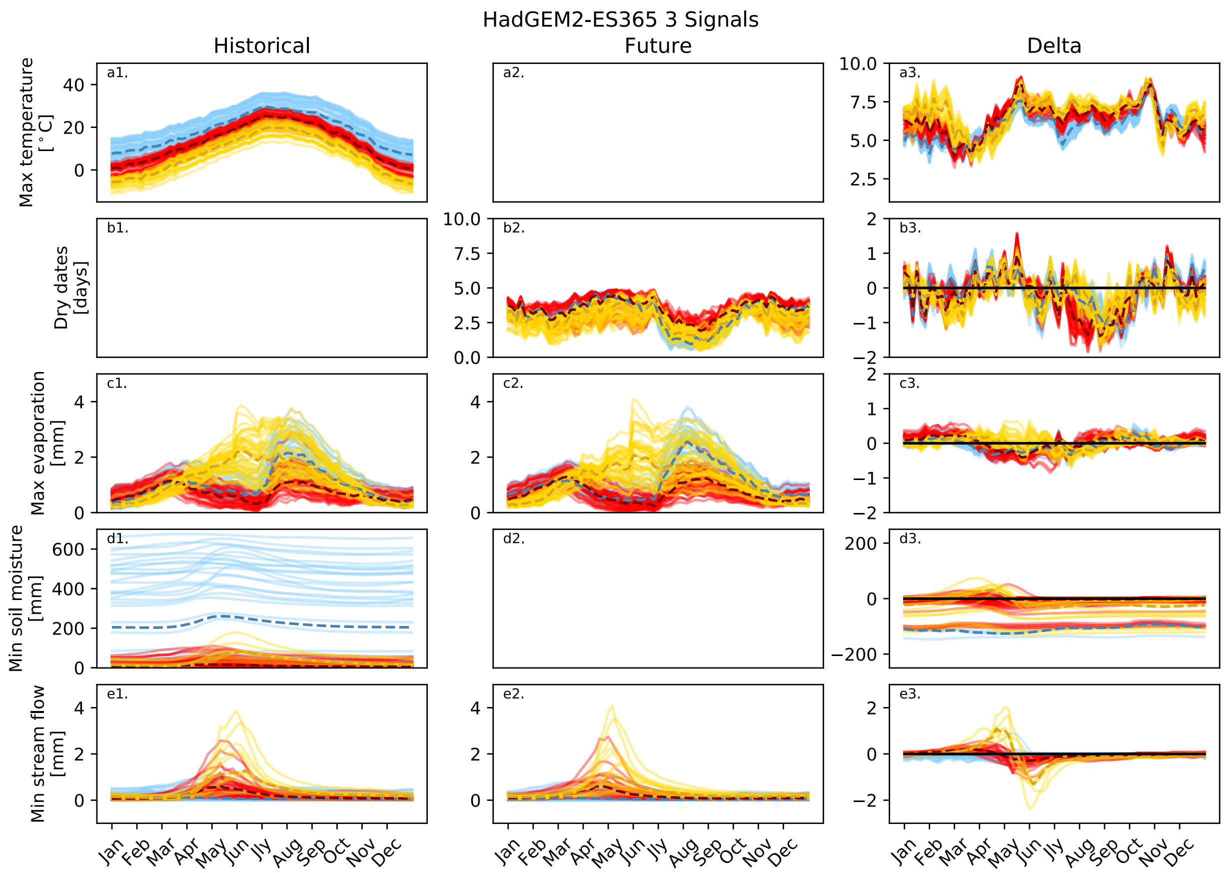

S5: Temporal results of the NMFk clustering at 3 signals for the HadGEM2-ES365 model for each time period and the ‘delta’ between historical and future.

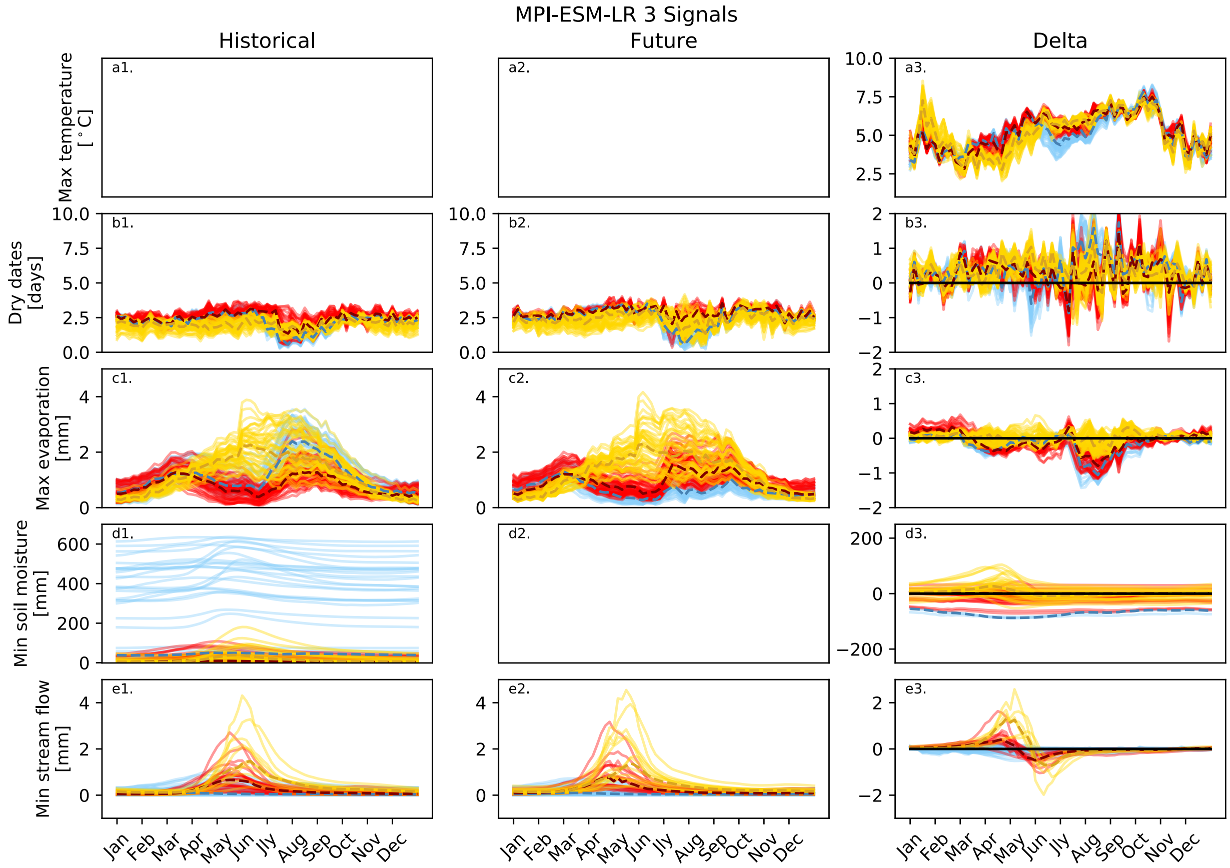

S6: Temporal results of the NMFk clustering at 3 signals for the MPI-ESM-LR model for each time period and the 'delta' between historical and future.

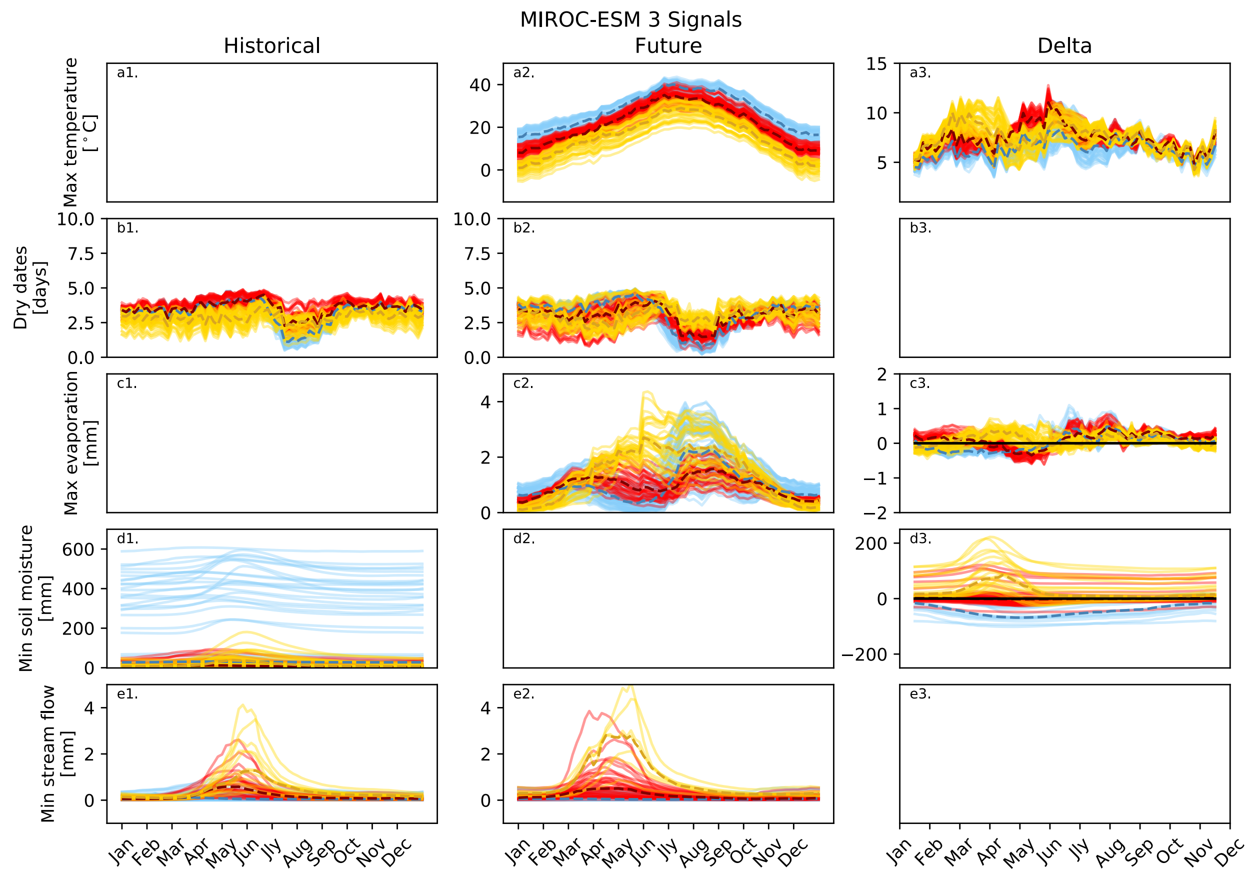

S7: Temporal results of the NMFk clustering at 3 signals for the MIROC-ESM model for each time period and the 'delta' between historical and future.

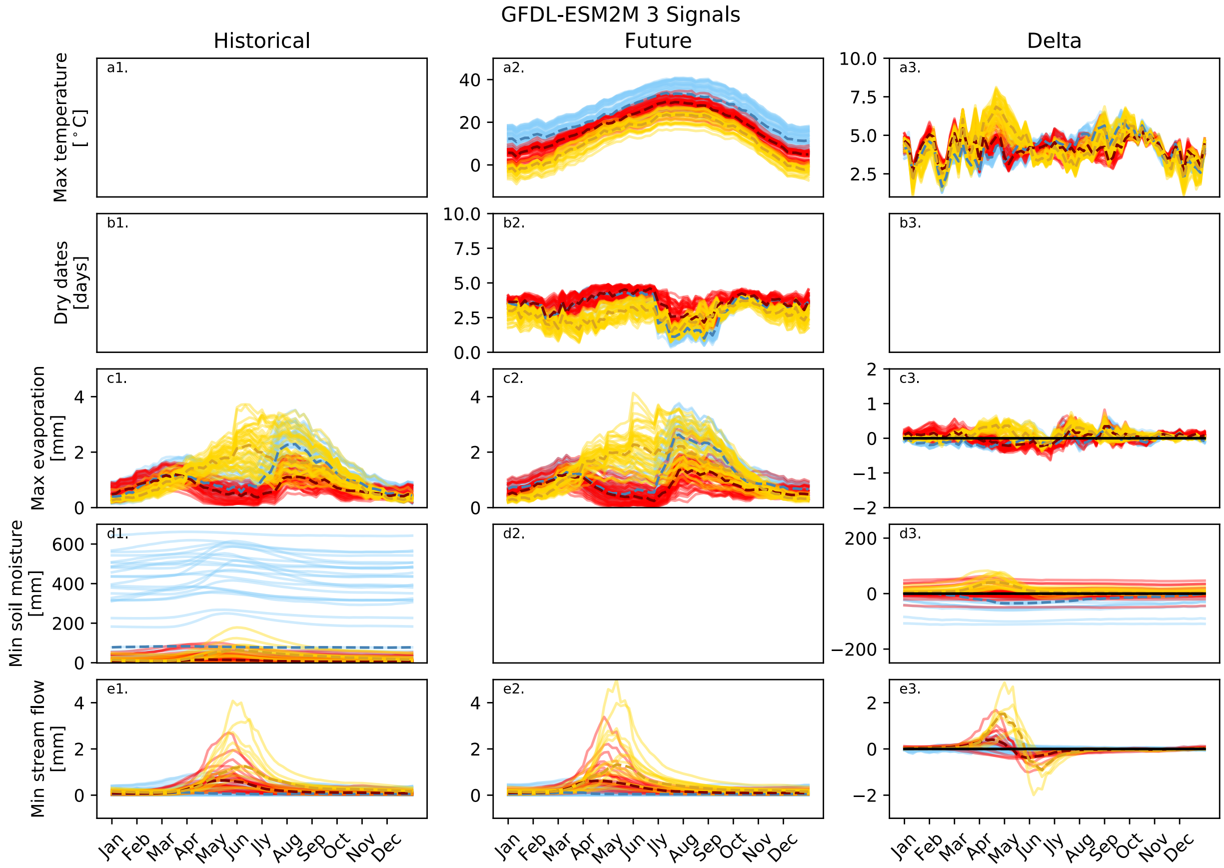

S8: Temporal results of the NMFk clustering at 3 signals for the GFDL-ESM2M model for each time period and the 'delta' between historical and future.

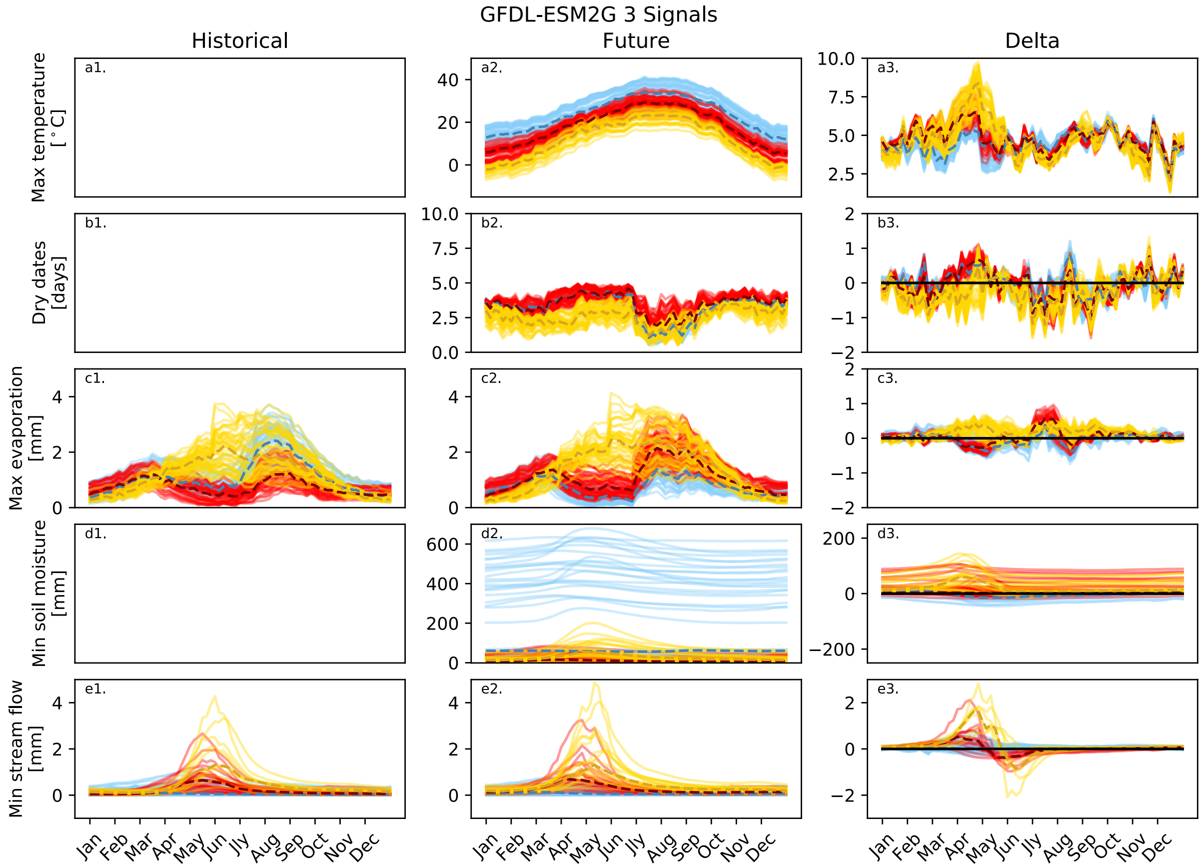

S9: Temporal results of the NMFk clustering at 3 signals for the GFDL-EMS2G model for each time period and the 'delta' between historical and future.

Characterizing Drought Behavior using Unsupervised Machine Learning for Improved Understanding of Future Drought in the Colorado River Basin

Carl J. Talsma[1], Katrina E. Bennett[1], Velimir V. Vesselinov[1]

[1] Earth and Environmental Sciences, Los Alamos National Laboratory, Los Alamos, NM, 87545.

Corresponding authors: Carl J. Talsma(talsmac83@lanl.gov), Velimir V. Vesselinov (vvv@lanl.gov)

Figure 1: The domain of the Colorado River Basin with adjacent areas that receive Colorado River water. Adapted from USGS, 2012 (accessed Jan 11th, 2021; USBR, 2012).

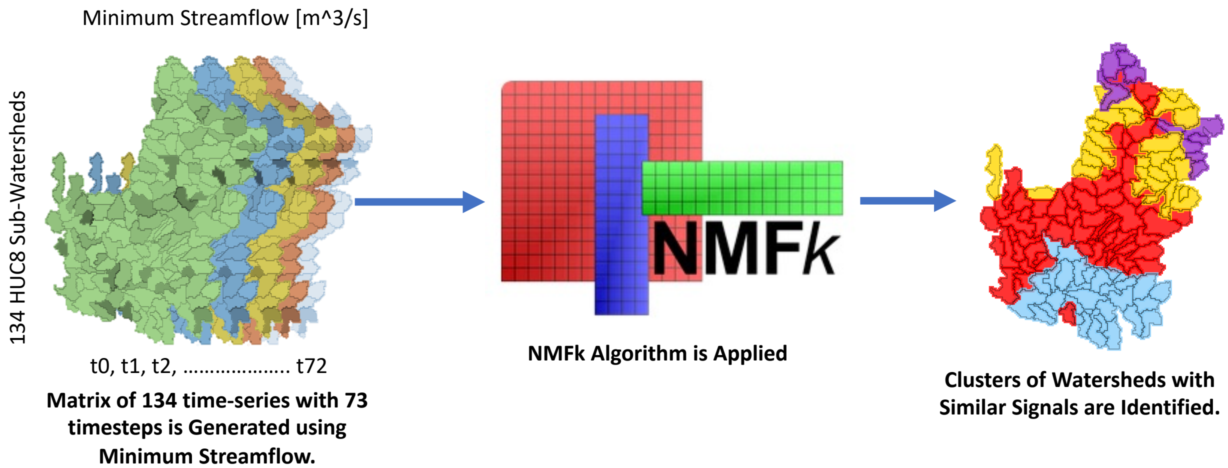

Figure 2: Process by which the NMFk algorithm is applied to the drough indicator data. A 2d matrix of minimum streamflow (*qn*) is created using the 134 HUC8 sub-watersheds with 73 5-day timesteps of streamflow throughout a year. This matrix is input into NMFk which clusters similar temporal signals of *qn* together.

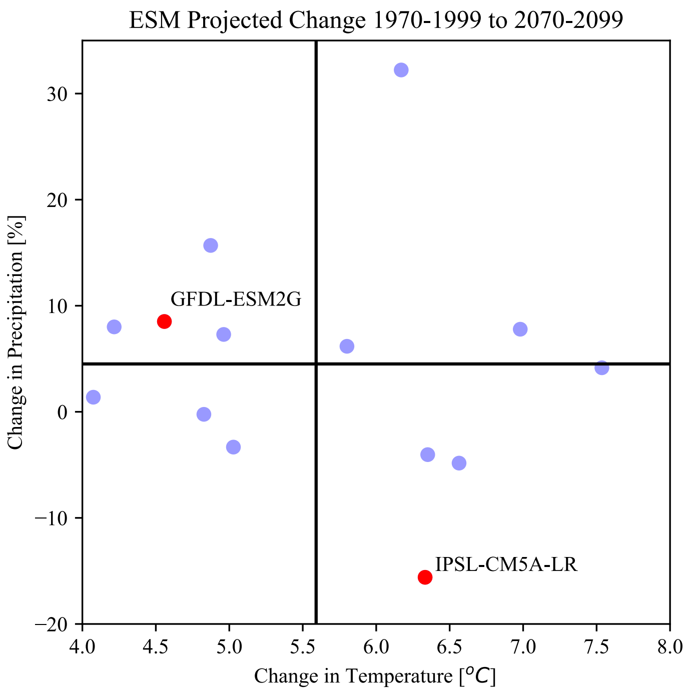

Figure 3: Average annual Precipitation changes (%) plotted against temperature changes (°C) for the CRB region for 14 different ESM's. GFDL-ESM2G and IPSL-CM5A-LR models are highlighted in red. Of the 14 ESMs, six were used in our analysis to cover the range of ESM results for precipitation and temperature change. Those six models are presented in the supplementary materials with the two highlighted models (GFDL-ESM2G and IPSL-CM5A-LR) discussed ind detail here. The vertical and horizontal black lines represent the multi-model mean of projected temperature and precipitation change, respectively.

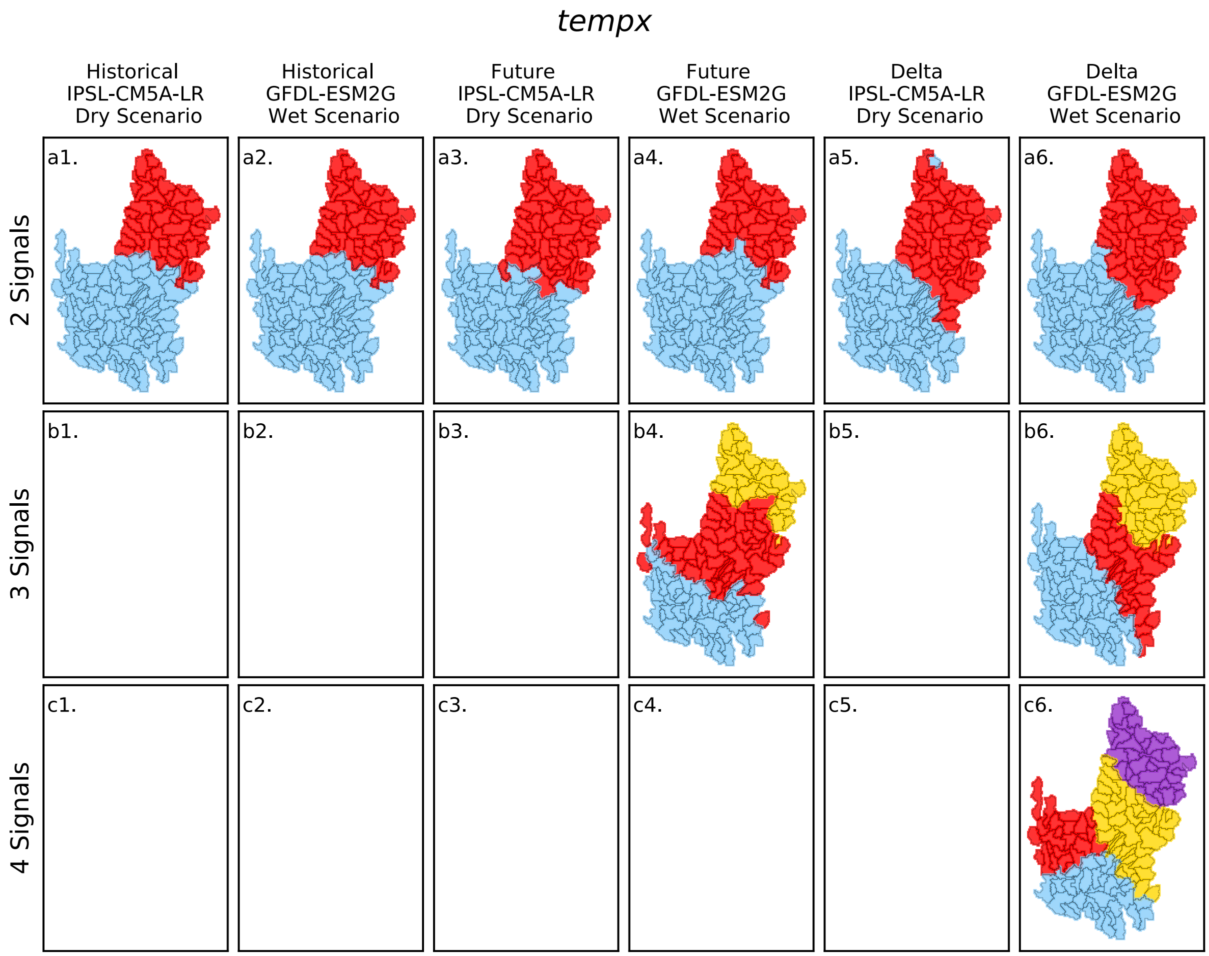

Figure 4: NFMk spatial grouping of HUC8 subsub-watersheds based on *tempx* dataset using solutions for 2, 3, and 4 extracted signals. The historical and future time periods, as well as the delta, are shown for both wet and dry scenarios. Each panel represents an independent NMFk clustering and the colors shown are not meaningful to one another across panels. Blank panels represent cases for each NMFk could not produce an acceptable solution.

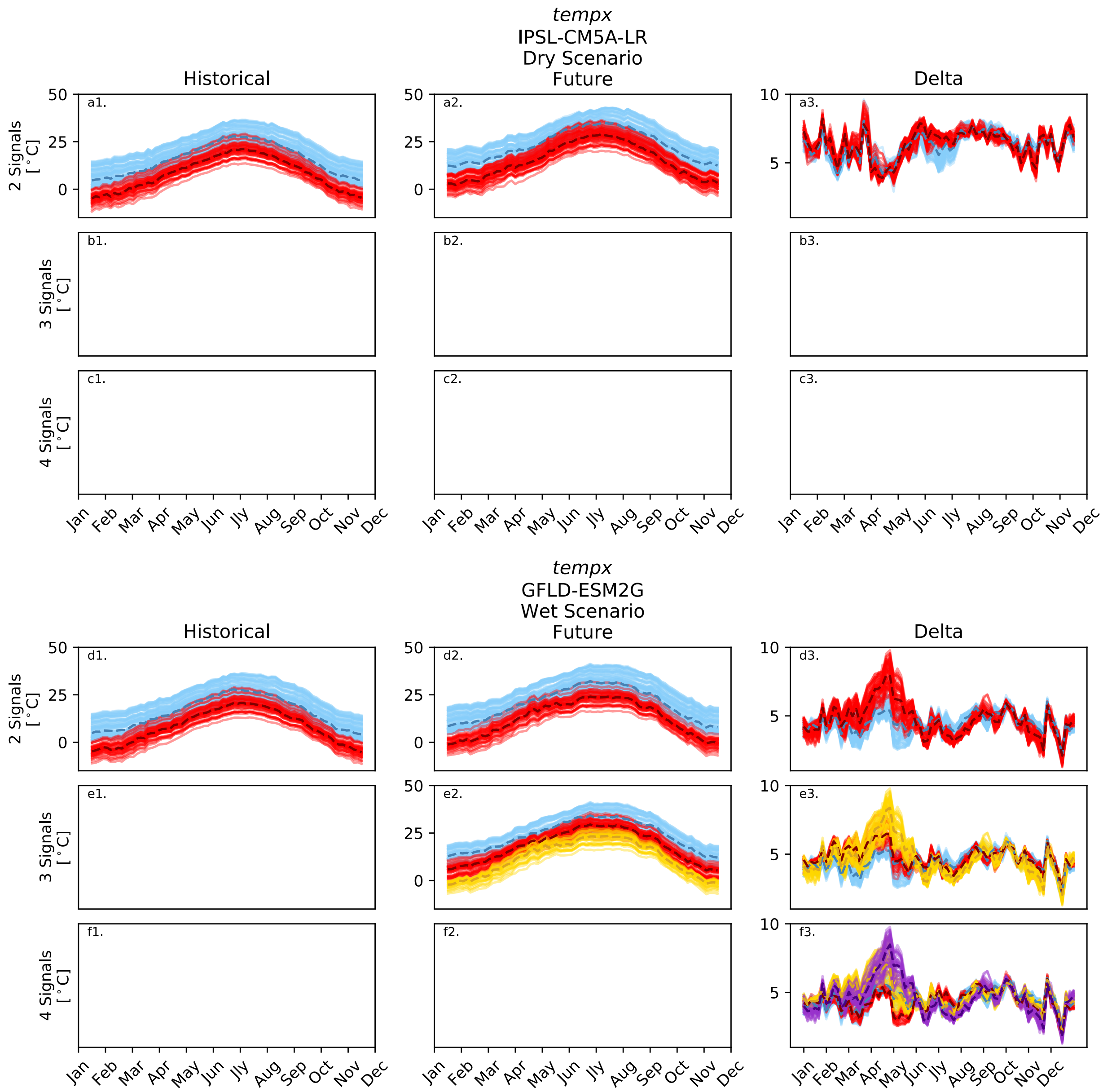

Figure 5: Temporal NFMk clustering of HUC8 subsub-watersheds based on the annual *tempx* signals for both IPSL-CM5A-LR (dry scenario) and GFDL-ESM2G (wet scenario) simulations. Solutions for 2, 3, and 4 extracted signals are presented for each time period. The clustering on this figure corresponds directly to the spatial clustering in the appropriate panels of Figure 3. Each line represents a single sub-watershed, while the dashed lines are representing the cluster medians at each time-step.

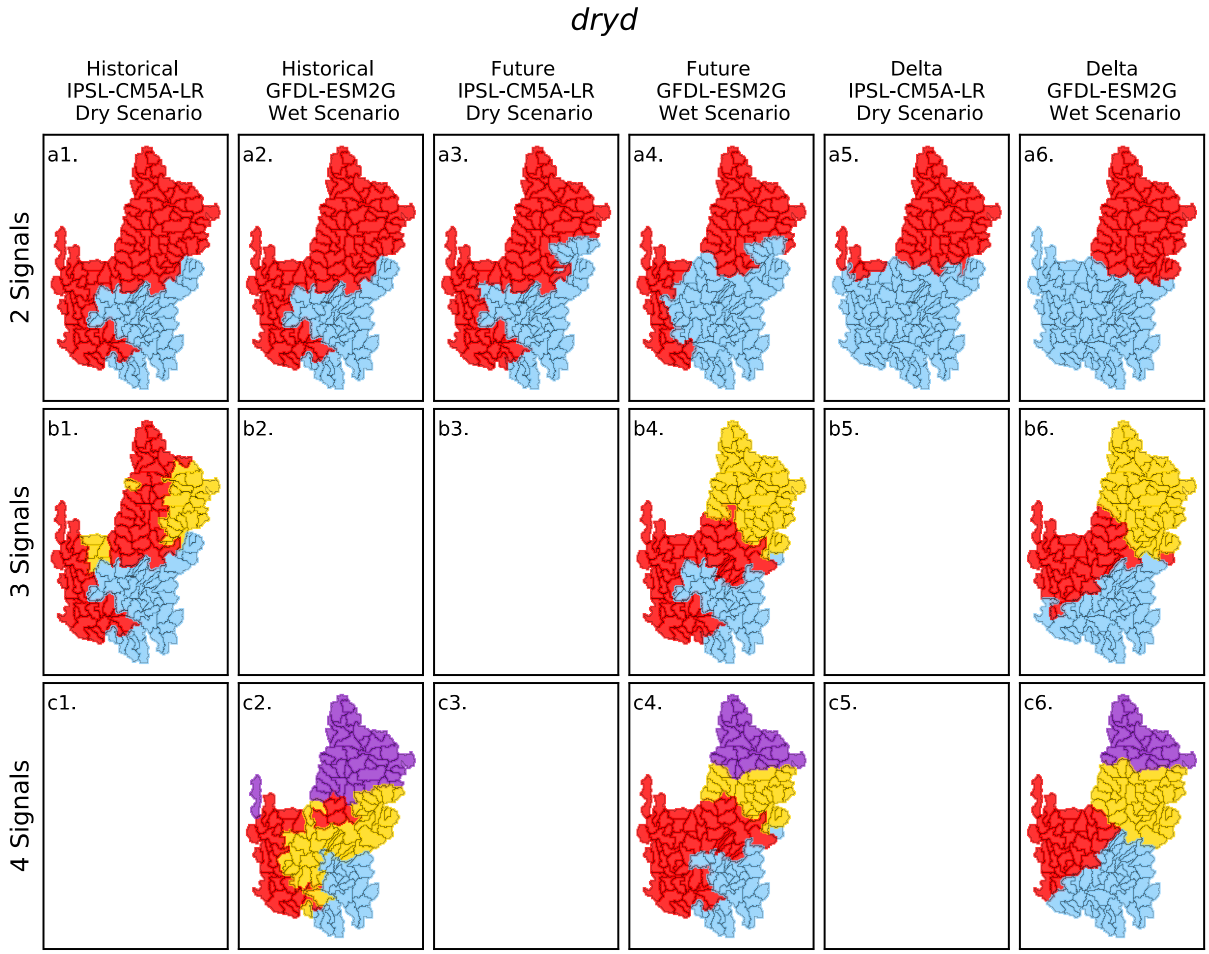

Figure 6: NFMk spatial grouping of HUC8 subsub-watersheds based on *dryd* dataset using solutions for 2, 3, and 4 extracted signals. The historical and future time periods, as well as the delta, are shown for both wet and dry scenarios. Each panel represents an independent NMFk clustering and the colors shown are not meaningful to one another across panels. Blank panels represent cases for each NMFk could not produce an acceptable solution.

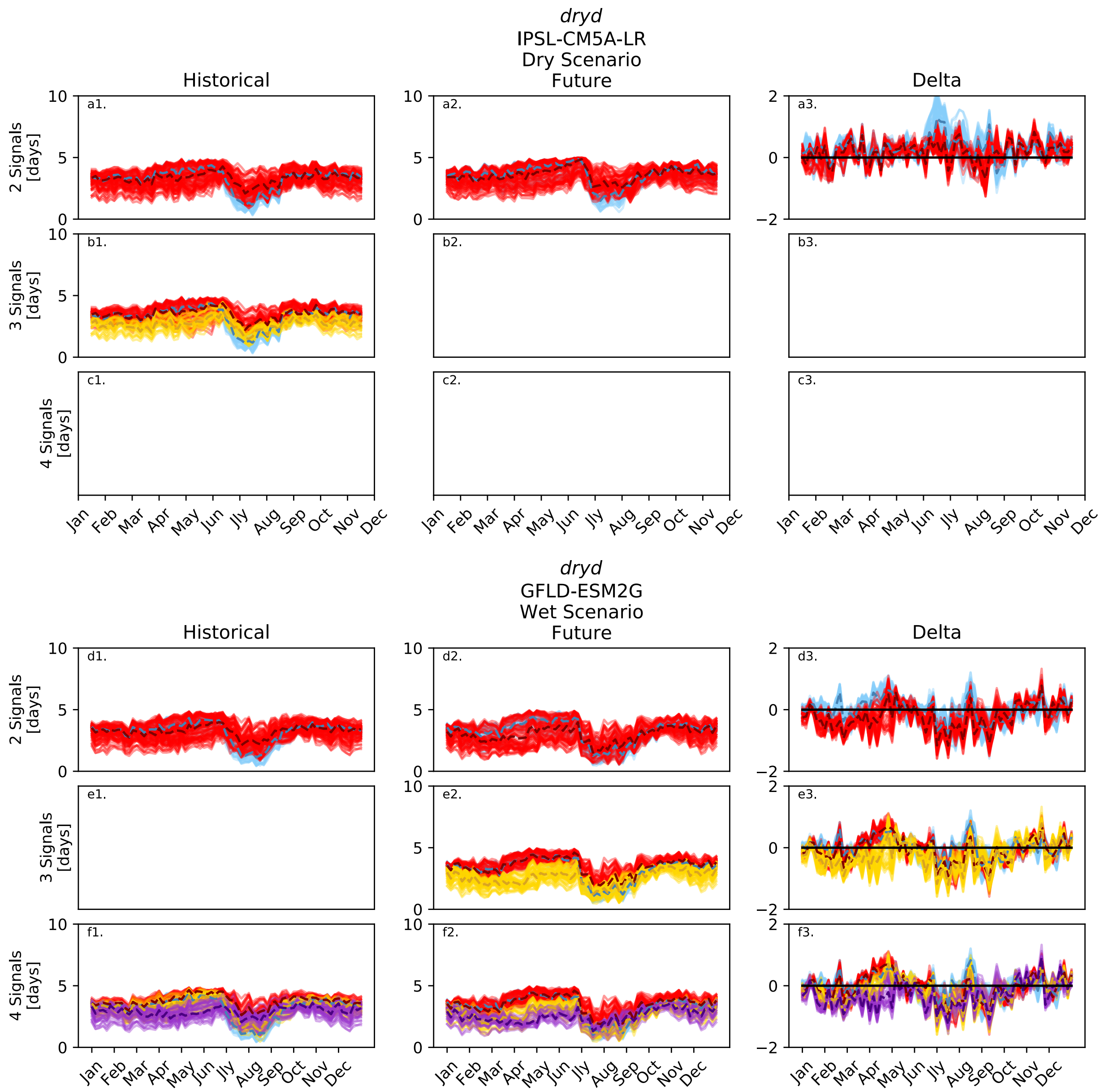

Figure 7: Temporal NFMk clustering of HUC8 subsub-watersheds based on the annual *dryd* signals for both IPSL-CM5A-LR (dry scenario) and GFDL-ESM2G (wet scenario) simulations. Solutions for 2, 3, and 4 extracted signals are presented for each time period. The clustering on this figure corresponds directly to the spatial clustering in the appropriate panels of Figure 3. Each line represents a single sub-watershed, while the dashed lines are representing the cluster medians at each time-step.

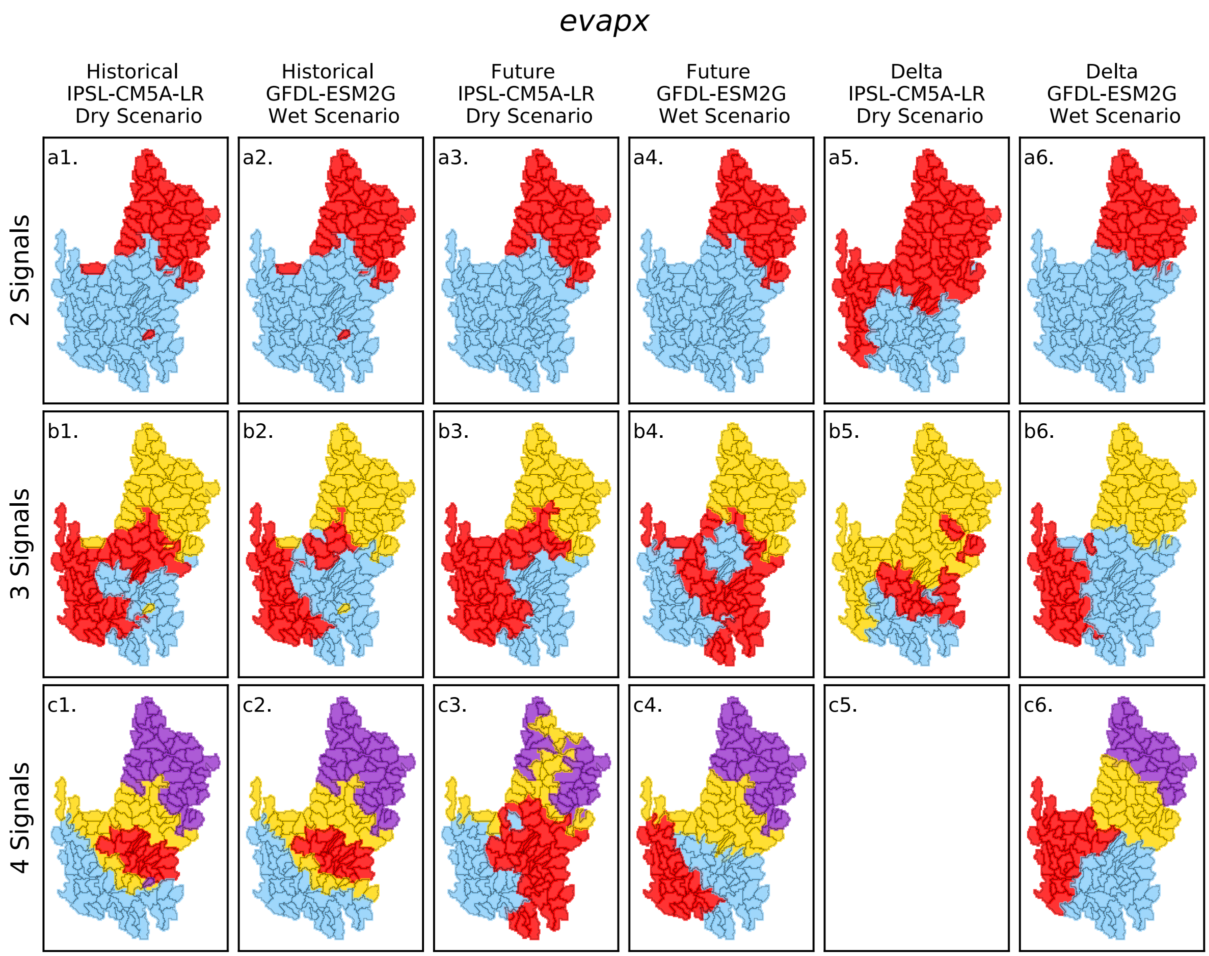

Figure 8: NFMk spatial grouping of HUC8 subsub-watersheds based on *evapx* dataset using solutions for 2, 3, and 4 extracted signals. The historical and future time periods, as well as the delta, are shown for both wet and dry scenarios. Each panel represents an independent NMFk clustering and the colors shown are not meaningful to one another across panels. Blank panels represent cases for each NMFk could not produce an acceptable solution.

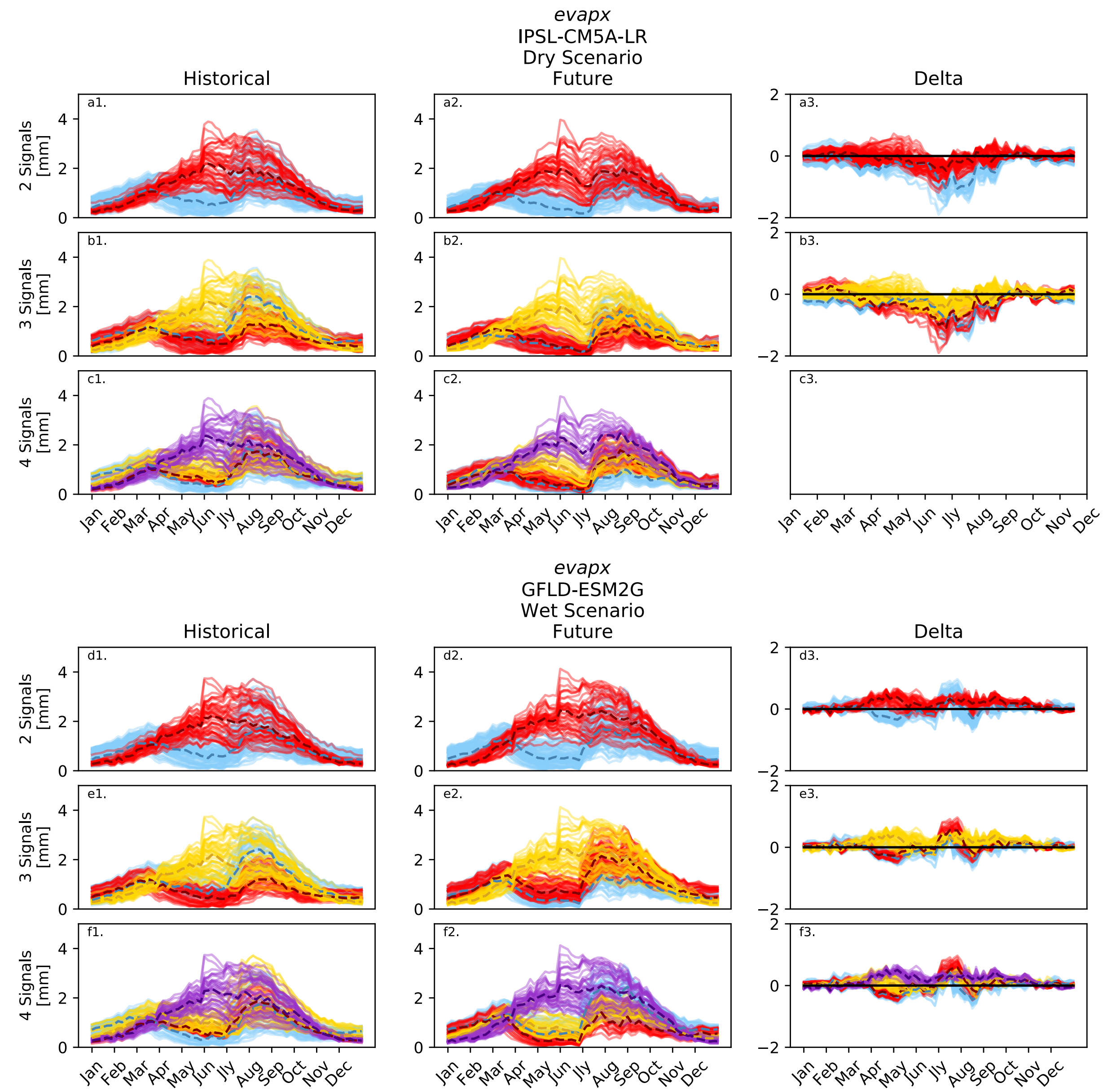

Figure 9: Temporal NFMk clustering of HUC8 subsub-watersheds based on the annual *evapx* signals for both IPSL-CM5A-LR (dry scenario) and GFDL-ESM2G (wet scenario) simulations. Solutions for 2, 3, and 4 extracted signals are presented for each time period. The clustering on this figure corresponds directly to the spatial clustering in the appropriate panels of Figure 3. Each line represents a single sub-watershed, while the dashed lines are representing the cluster medians at each time-step.

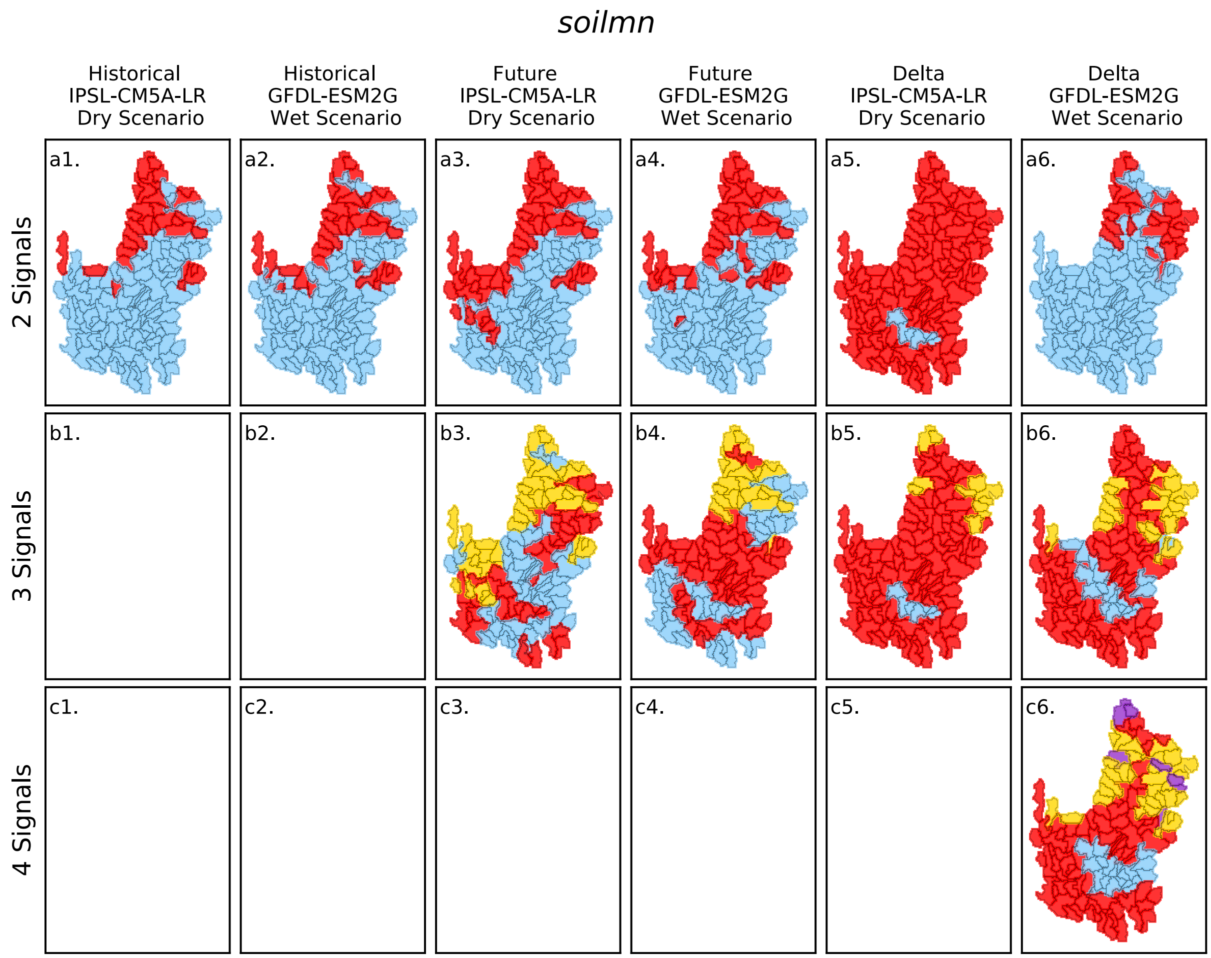

Figure 10: NFMk spatial grouping of HUC8 subsub-watersheds based on *soilmn* dataset using solutions for 2, 3, and 4 extracted signals. The historical and future time periods, as well as the delta, are shown for both wet and dry scenarios. Each panel represents an independent NMFk clustering and the colors shown are not meaningful to one another across panels. Blank panels represent cases for each NMFk could not produce an acceptable solution..

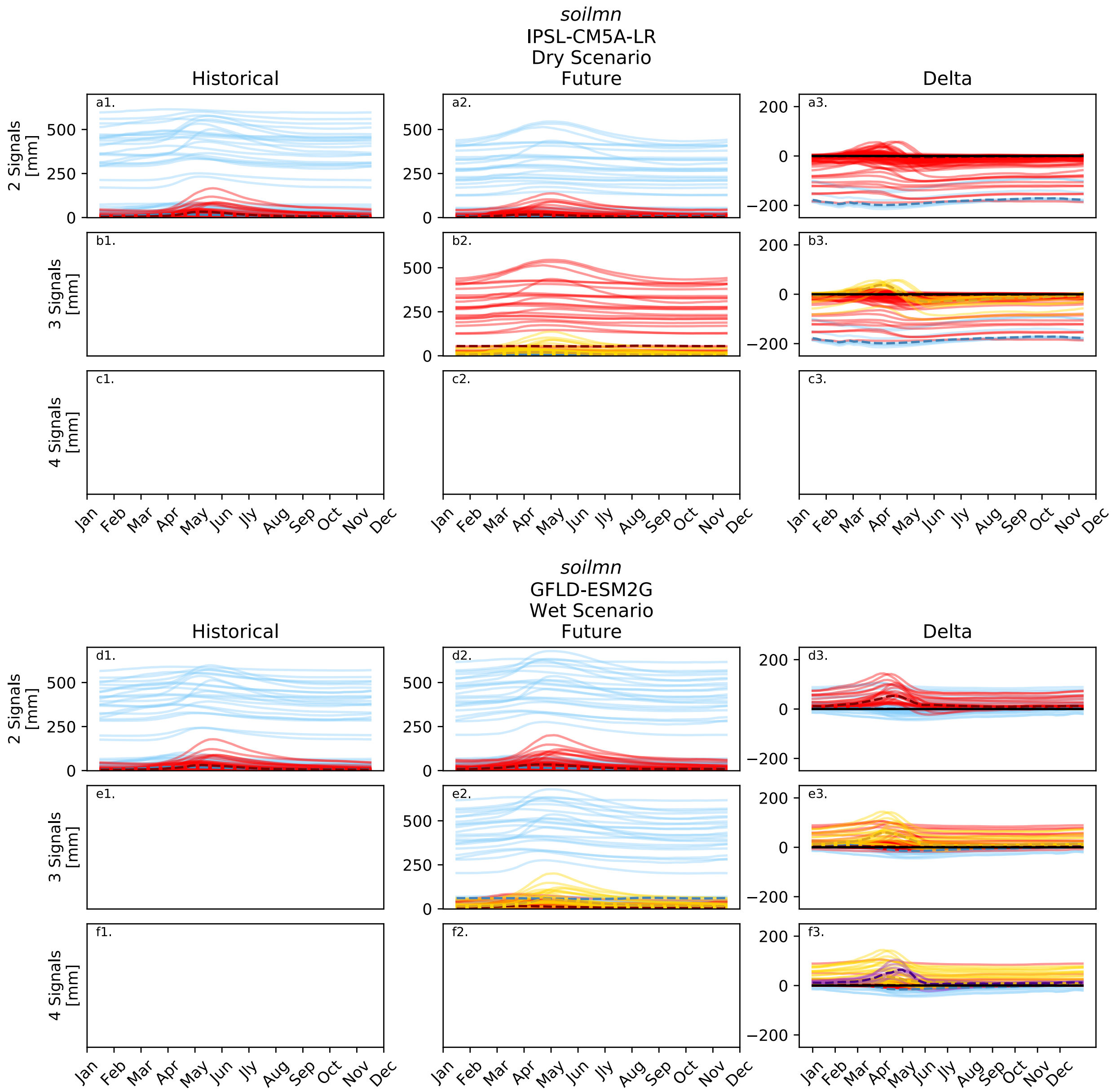

Figure 11: Temporal NFMk clustering of HUC8 subsub-watersheds based on the annual *soilmn* signals for both IPSL-CM5A-LR (dry scenario) and GFDL-ESM2G (wet scenario) simulations. Solutions for 2, 3, and 4 extracted signals are presented for each time period. The clustering on this figure corresponds directly to the spatial clustering in the appropriate panels of Figure 3. Each line represents a single sub-watershed, while the dashed lines are representing the cluster medians at each time-step.

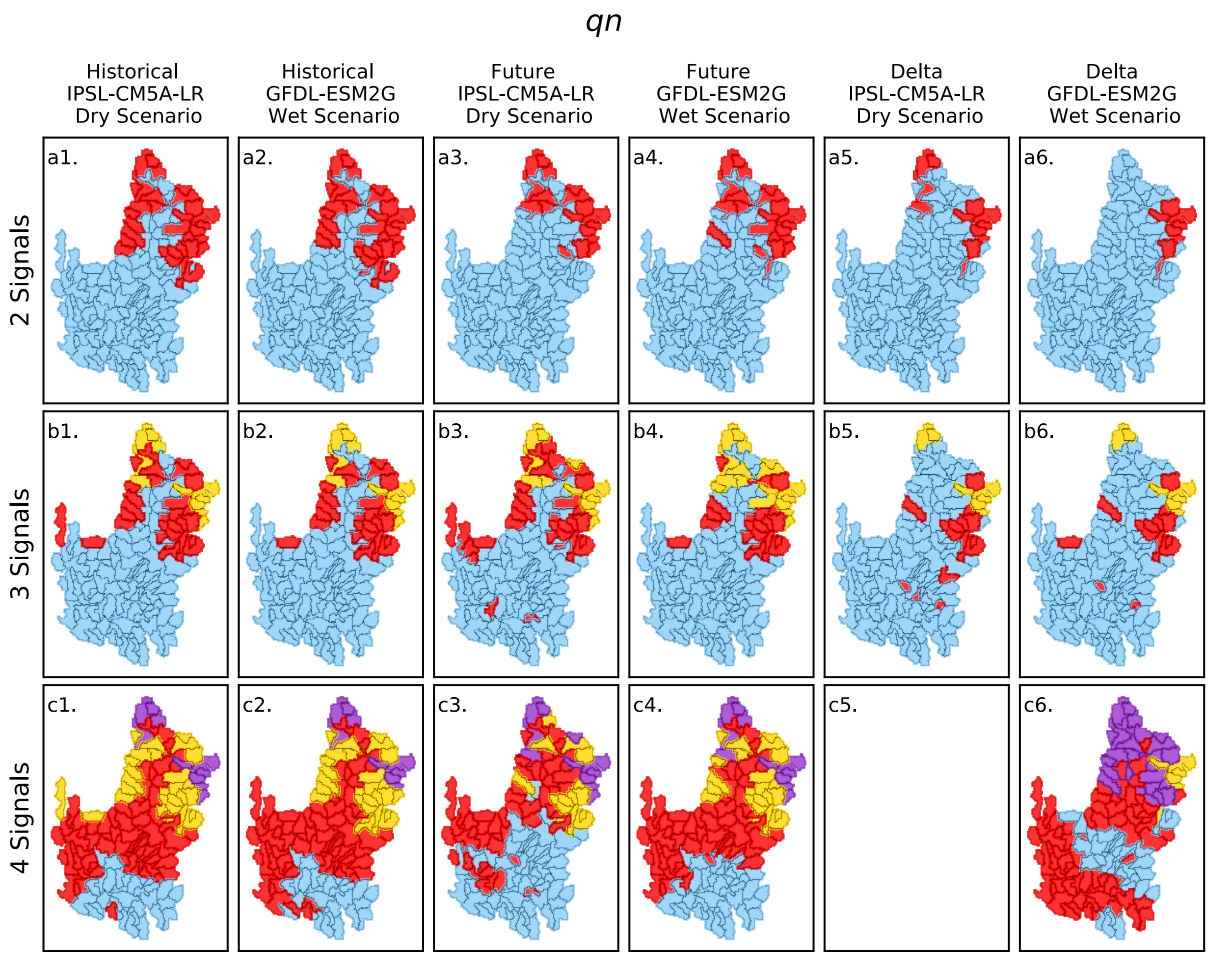

Figure 12: NFMk spatial grouping of HUC8 subsub-watersheds based on *qn* dataset using solutions for 2, 3, and 4 extracted signals. The historical and future time periods, as well as the delta, are shown for both wet and dry scenarios. Each panel represents an independent NMFk clustering and the colors shown are not meaningful to one another across panels. Blank panels represent cases for each NMFk could not produce an acceptable solution.

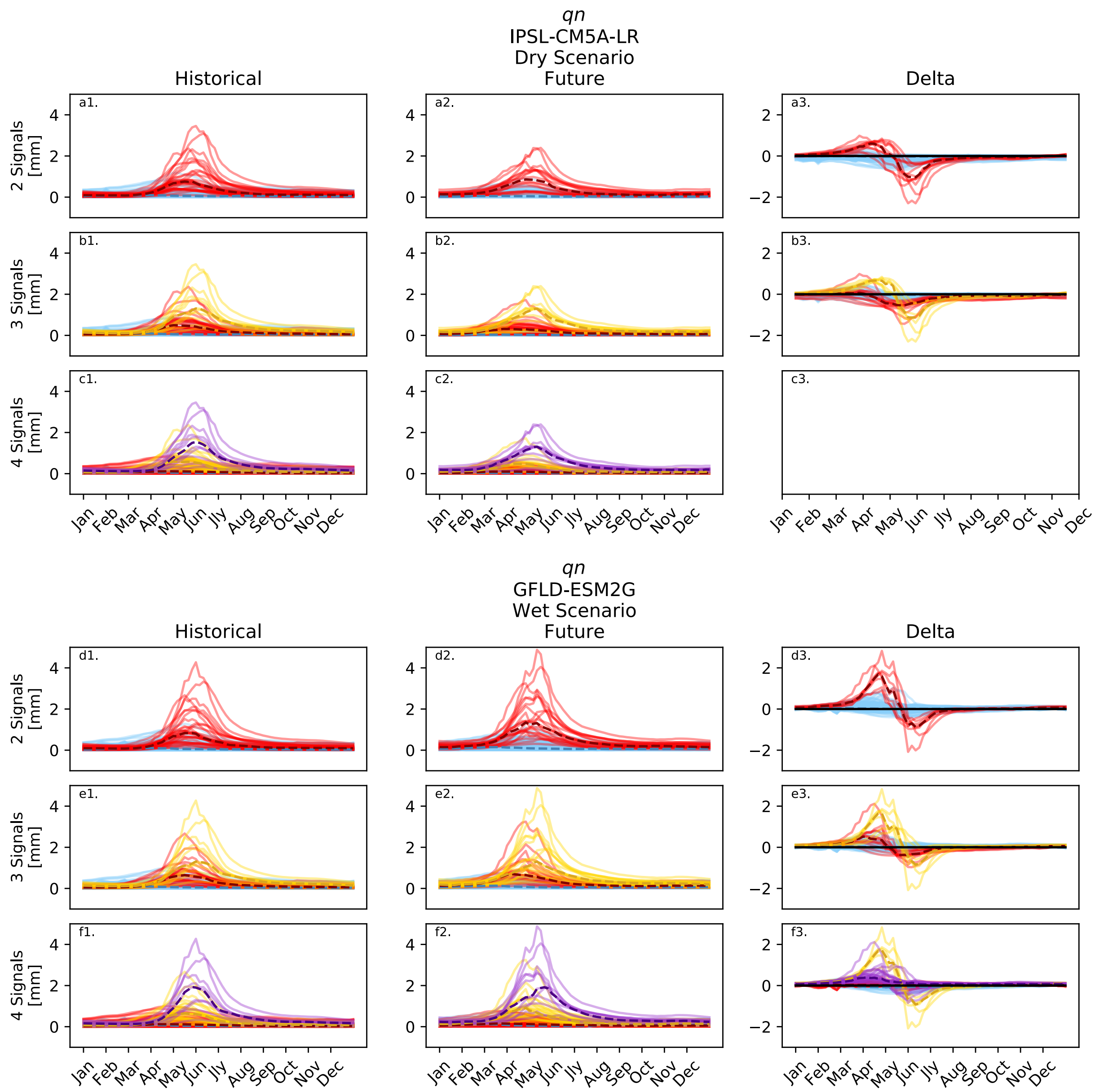

Figure 13: Temporal NFMk clustering of HUC8 subsub-watersheds based on the annual *qn* signals for both IPSL-CM5A-LR (dry scenario) and GFDL-ESM2G (wet scenario) simulations. Solutions for 2, 3, and 4 extracted signals are presented for each time period. The clustering on this figure corresponds directly to the spatial clustering in the appropriate panels of Figure 3. Each line represents a single sub-watershed, while the dashed lines are representing the cluster medians at each time-step.

	ΔT (℃)	ΔP (%)
IPSL-CM5A-LR	**6.33**	**-15.60**
HadGEM2-ES365	6.35	-4.04
MPI-ESM-LR	5.03	-3.33
GFDL-ESM2M	4.07	1.38
MIROC-ESM	6.98	7.79
GFDL-ESM2G	**4.56**	**8.51**

Table 1: Projected change in mean annual temperature and precipitation in the CRB simulated using the six ESM models used in this study. IPSL-CM5A-lR and GFDL-ESM2G are in bold and are discussed in detail in this study while the other models are presented in the supplementary materials.